

# **PRE-PRINT**

## **Influence of zones of pre-existing crustal weakness on strain localization and partitioning during rifting: Insights from analogue modeling using high resolution 3D digital image correlation**

**Edoseghe E. Osagiede<sup>1,2,\*</sup>, Matthias Rosenau<sup>3</sup>, Atle Rotevatn<sup>1</sup>, Rob Gawthorpe<sup>1</sup>, Christopher A-L. Jackson<sup>4</sup>, and Michael Rudolf<sup>3</sup>**

<sup>1</sup>Geodynamics and Basin Studies Group, Department of Earth Science, University of Bergen, Allégaten 41, 5007, Bergen, Norway.

<sup>2</sup>Department of Geology, University of Benin, PMB 1154, Benin City, Nigeria.

<sup>3</sup>Lithosphere Dynamics, Helmholtz Centre Potsdam, German Research Centre for Geosciences (GFZ), Telegraphenberg, D-14473 Potsdam, Germany.

<sup>4</sup>Basins Group, Department of Earth and Environmental Sciences, The University of Manchester, Williamson Building, Oxford Road, Manchester, M13 9PL, United Kingdom.

Corresponding author: Edoseghe Edwin Osagiede ([edoseghe.osagiede@uib.no](mailto:edoseghe.osagiede@uib.no); [edoseghe.osagiede@uniben.edu](mailto:edoseghe.osagiede@uniben.edu))

***This manuscript has been submitted to TECTONICS. Please note that the manuscript has not undergone peer review yet. Subsequent versions of this manuscript may have slightly different content.***



## 22 **Abstract**

23 Pre-existing crustal structures have been shown to influence rifting, but the factors controlling  
24 their influence remain poorly understood. We present the results of surface strain analysis of a  
25 series of analogue rifting experiments designed to test the influence of the size, orientation,  
26 depth, and geometry of pre-existing crustal weak zones on strain localization and partitioning.  
27 We apply distributed basal extension to crustal-scale models which consist of a silicone weak  
28 zone embedded in a quartz sand layer. We vary the size and orientation ( $\theta$ -angle) of the weak  
29 zone with respect to the extension direction, reduce the thickness of the sand layer to simulate  
30 a shallow weak zone, and vary the geometry of the weak zone. Our results show that at higher  
31  $\theta$ -angle ( $\leq 60^\circ$ ) both small- and large-scale weak zones localize strain into graben-bounding  
32 (oblique-) normal faults. At lower  $\theta$ -angle ( $\leq 45^\circ$ ), small-scale weak zones do not localize strain  
33 effectively, unless they are shallow. In most models, we observe diffuse, second-order strike-  
34 slip internal graben structures, which are conjugate and antithetic under orthogonal and oblique  
35 extension, respectively. In general, the changing nature of the rift faults (from discrete fault  
36 planes to diffuse fault zones, from normal to oblique and strike-slip) highlights the sensitivity  
37 of rift architecture to the orientation, size, depth, and geometry of pre-existing weak zones. Our  
38 generic models are comparable to observations from many natural rift systems like the northern  
39 North Sea and East Africa, and thus have implications for understanding the role of structural  
40 inheritance in rift basins globally.

## 41 **1 Introduction**

42 Intra-continental rifting very commonly occurs along pre-existing crustal heterogeneities (e.g.,  
43 McConnell, 1967; Dunbar & Sawyer, 1988; Daly et al., 1989; Versfelt & Rosendahl, 1989;  
44 Ring, 1994; Vauchez et al., 1998; Corti et al., 2003; Gibson et al., 2013; Brune et al., 2017).  
45 Such presumably weak heterogeneities include discrete faults (with limited width), diffuse  
46 shear zones (up to several 10s of km-wide) and mobile belts (up to 100s of km-wide), and  
47 orogenic structural templates, all of which create crustal-scale rheological and mechanical  
48 anisotropies (e.g., Daly et al., 1989; Ranalli & Yin, 1990). Numerous subsurface- and field-  
49 based studies suggest such pre-existing structures can influence the location, orientation,  
50 dimensions, segmentation, and interaction of subsequent rift-related structures (e.g., Daly et al.,  
51 1989; Bartholomew et al., 1993; Maurin & Guiraud, 1993; Maerten et al., 2002; Morley et al.,  
52 2004; Morley, 2010; Kirkpatrick et al., 2013; Fazlikhani & Back, 2015; Salomon et al., 2015;  
53 de Castro et al., 2016; Phillips et al., 2016; Fazlikhani et al., 2017; Dawson et al., 2018;  
54 Kolawole et al., 2018; Muirhead & Kattenhorn, 2018; Rotevatn et al., 2018; Collanega et al.,  
55 2019; Heilman et al., 2019; Osagiede et al., 2020a).

56 In many natural rifts like the northern North Sea Rift (e.g., Reeve et al., 2015; Phillips et al.,  
57 2016; Claringbould et al., 2017; Phillips et al., 2019; Osagiede et al., 2020a), East African Rift  
58 System (e.g., Daly et al., 1989; Morley, 1995; Heilman et al., 2019), Parnaíba Basin, Brazil (de  
59 Castro et al., 2016), Thailand rift basins (Morley et al., 2004), and East Greenland Rift System  
60 (e.g., Rotevatn et al., 2018), the influence of pre-existing crustal structures on strain localization  
61 during extension varies, (see Fig. 1). Whereas some pre-existing crustal structures clearly  
62 reactivate and control subsequent deformation, others seem to have limited or no influence. It  
63 is this variable effect of pre-existing structures on younger rift-related structures that we here  
64 refer to as *selective influence*. Although the influence of pre-existing crustal structures on strain

65 localization in natural rifts is well recognized, the factors that control their observed selective  
66 influence remain poorly understood. Seismic reflection data suggest that the thickness and, to  
67 some extent, the depth of pre-existing crustal structures like shear zones seem to dictate their  
68 influence on the superposed rift structures (e.g., Reeve et al., 2013; Phillips et al., 2016;  
69 Osagiede et al., 2020a). Analogue and numerical simulations of rift processes provide valuable  
70 tools to validate such hypotheses.

71 *Insert Figure 1*

72 Scaled analogue or numerical models allow us to monitor the progressive crustal strain  
73 localization process and the development of rifts at high resolution in space and time. Over the  
74 past decades a growing number of analogue- (e.g., Withjack & Jamison, 1986; Allemand &  
75 Brun, 1991; Tron & Brun, 1991; Dauteuil & Brun, 1993; McClay & White, 1995; Bonini et al.,  
76 1997; Keep & McClay, 1997; Basile & Brun, 1999; Brun, 1999; Clifton et al., 2000; Michon  
77 & Merle, 2000; Corti et al., 2001; Chemenda et al., 2002; McClay et al., 2002; Bellahsen et al.,  
78 2003; Corti et al., 2003; Bellahsen & Daniel, 2005; Michon & Sokoutis, 2005; Sokoutis et al.,  
79 2007; Agostini et al., 2009; Autin et al., 2010; Henza et al., 2010; Aanyu & Koehn, 2011;  
80 Agostini et al., 2011; Autin et al., 2013; Chattopadhyay & Chakra, 2013; Tong et al., 2014;  
81 Bonini et al., 2015; Philippon et al., 2015; Zwaan et al., 2016; Zwaan & Schreurs, 2017; Molnar  
82 et al., 2019; Sani et al., 2019; Zwaan et al., 2019; Ghosh et al., 2020; Maestrelli et al., 2020;  
83 Molnar et al., 2020) and numerical- (e.g., Van Wijk, 2005; Dyksterhuis et al., 2007; Maniatis  
84 & Hampel, 2008; Allken et al., 2012; Brune et al., 2012; Brune & Autin, 2013; Brune, 2014;  
85 Brune et al., 2017; Deng et al., 2017; Duclaux et al., 2020) modeling studies have investigated  
86 the role of pre-existing structures on evolving rifts, addressing the role of orthogonal and  
87 oblique extension, and the effect of the orientation of pre-existing crustal and/or mantle

88 weaknesses, the thickness of the brittle layer, brittle-ductile coupling, the presence or absence  
89 of weak lower crust, extension velocity, and multi-phase extension.

90 Most previous studies have focused on first-order attributes like the nature of pre-existing weak  
91 structures such as discrete (faults) versus distributed structures (e.g., Bellahsen & Daniel, 2005;  
92 Tong et al., 2014; Bonini et al., 2015; Deng et al., 2017), and the orientation (obliquity) of the  
93 inherited structure with regards to the extension direction (e.g., Withjack & Jamison, 1986;  
94 McClay & White, 1995; Michon & Sokoutis, 2005; Agostini et al., 2009; Autin et al., 2013;  
95 Molnar et al., 2019). With the progress made in seismic imaging of deeply buried structures  
96 located in crystalline basement, higher-order attributes such as the size, depth and shape of pre-  
97 existing structures are becoming evident (e.g., Phillips et al., 2016; Wrona et al., 2020; Osagiede  
98 et al., 2020a); such attributes have received little attention in modeling studies, thus little is  
99 known about how they influence the evolving rifts, especially in the context of pre-existing  
100 structures like crustal shear zones (here referred to as weak zones).

101 In this study, we investigate the controls that pre-existing crustal weak zones have on the strain  
102 localization process and development of rift-related structures during extension. We achieve  
103 this through a series of extensional analogue experiments that test how the (i) size, (ii) depth,  
104 and (iii) geometry of pre-existing crustal weak zones (specifically shear zones) affect their  
105 propensity to influence younger rift faults. We deploy state-of-the-art stereoscopic (3D) digital  
106 image correlation (DIC) technique that allows us to quantitatively assess the evolution of the  
107 model surface deformation and structural pattern at high resolution. Our results are of generic  
108 significance and have implications for understanding how pre-existing weak zones selectively  
109 influence younger rift faults in natural rift systems.

## 110 **2 Experimental method and model design**

### 111 **2.1 Experimental setup**

112 The experimental apparatus can be considered a pure shear extension experiment (Fig. 2). A  
113 basal neoprene foam block with dimensions of 50 x 50 x 12 cm is first compressed by 5 cm (i.e.  
114 down to an initial width of 45 cm) between a fixed and mobile wall, with open side walls, before  
115 placing the rock analogue materials on top of it. Subsequently, we start the model run by slowly  
116 moving the mobile wall at a constant rate of 0.005 mm/s, and releasing the compressed foam  
117 by a total of 5 cm, translating theoretically into c. 11% of extension during each model run. Due  
118 to some localization of extension at the model boundaries, the effective extension in the model  
119 domain is a bit less (c.  $9 \pm 1\%$ ) and distributed homogeneously as verified by benchmarks  
120 (Appendix 1). The use of a basal foam in analogue model studies has the advantage of  
121 simulating distributed extension with a constant basal velocity gradient (Appendix 1),  
122 compared to the use of rigid base plates that typically serve to strongly localize basal extension  
123 (e.g., Schlagenhauf et al., 2008; Zwaan et al., 2019).

124 A side effect of using elastic materials to impose basal kinematic boundary conditions is the  
125 association of transverse contraction along with longitudinal extension. This “Poisson’s effect”  
126 may lead to a switch in simulated tectonic setting from crustal extension to strike-slip if the  
127 Poisson’s ratio is close to 50%, as often happens with a basal rubber sheet, for example  
128 (Bahroudi et al., 2003; Zwaan et al., 2019). However, in our model setup, lateral contraction of  
129 the basal foam block is c. 16% of its longitudinal extension (i.e., 0.8 cm contraction associated  
130 with 5 cm extension, Appendix 1) and therefore suitable for simulating crustal extension with  
131 only a minor contribution of transverse contraction.

132 In this study, our focus is on the surface deformation of the brittle crust; we do not explicitly  
133 model a ductile lower crust, which has been sufficiently addressed by previous analogue

134 modeling studies (e.g., Allemand & Brun, 1991; Brun, 1999; Bellahsen et al., 2003; Zwaan et  
135 al., 2019). Our reference model setup therefore simulates an old and cold stable (e.g., Brun,  
136 1999; Zwaan et al., 2019) or a highly coupled (e.g., Dyksterhuis et al., 2007) crustal/lithospheric  
137 setting. That is, our model setup does not capture the vertical rheological stratification that may  
138 characterize the crust, but rather focus on the lateral mechanical anisotropy induced by  
139 relatively local pre-existing weak zones like shear zones (e.g., Vauchez et al., 1998).

140 *Insert Figure 2*

## 141 **2.2 Rock analogue materials**

142 As a rock analogue material for the brittle upper crust, we used a mix of natural- and a few  
143 percent of black-colored, dry, quartz sand (type G12, Rosenau et al., 2018). This mixture  
144 provides an appropriate visual contrast that allows for the digital correlation of recorded images  
145 (e.g., White et al., 2001). The grain size is 100 – 400  $\mu\text{m}$ , with an average of 240  $\mu\text{m}$ . The bulk  
146 density of the sieved sand is about 1700  $\text{kg}/\text{m}^3$ . The sand exhibits a frictional-Coulomb plastic  
147 behavior, with static and dynamic friction coefficients of 0.69 and 0.55, respectively, and a  
148 cohesion in the order of a few tens of Pascal (see Table 1) (Rosenau et al., 2018). Quartz sand  
149 like this has been widely used to represent brittle upper crustal rocks in numerous analogue  
150 models (Lohrmann et al., 2003; Adam et al., 2005; Panien et al., 2006; Schreurs et al., 2006,  
151 2016; Klinkmüller et al., 2016; Ritter et al., 2016; Schellart & Strak, 2016; Del Ventisette et al.,  
152 2019).

153 We use viscoelastic objects made of Polydimethylsiloxane (PDMS) or silicone oil to represent  
154 pre-existing weak zones, simulating kilometer-scale shear zones within the brittle crust. While  
155 several methods permit simulation of weak zones into sand-based analogue models (e.g., Le  
156 Calvez & Vendeville, 2002; Zwaan et al., 2019), a major advantage of using silicone oil is that  
157 it can be easily moulded to produce a range of sizes and shapes that reflects a diverse range of



158 natural weak zone geometries. The silicone oil has a density ( $\rho$ ) of c.  $960 \text{ kg/m}^3$ , and a zero-  
159 shear viscosity ( $\eta$ ) of c.  $2.24 \times 10^4 \text{ Pa s}$  (Table 1) (Rudolf et al., 2016). As a Maxwell viscoelastic  
160 fluid, it has a linear viscous rheology (Newtonian) at relatively low strain rates as realized in  
161 our experiments, changing to a non-linear viscous rheology at much higher strain rates than  
162 achieved in this study (Rudolf et al., 2016). We choose this material for the weak zone because  
163 it can respond to the extension applied at the model base while maintaining its shape and height  
164 over the experimental time scale.

165 *Table 1: Material properties*

<b>Brittle Layer (granular material)</b>	<b>Quartz Sand 'G12'</b>
Grain size range ( $\mu\text{m}$ ) <sup>a</sup>	100-400
Mean grain size ( $\mu\text{m}$ ) <sup>a</sup>	240
Grain density ( $\text{kg/m}^3$ ) <sup>a</sup>	2650
Sieved density ( $\text{kg/m}^3$ ) <sup>a</sup>	1700
Coefficient <sup>a</sup> /Angle of internal peak friction	0.69/34.6°
Coefficient <sup>a</sup> /Angle of internal dynamic (sliding) friction	0.55/28.8°
Strain softening (%)	20
Cohesion (Pa) <sup>a</sup>	50 - 110
<b>Weak zone (viscous material)</b>	<b>Polydimethylsiloxane (PDMS) KORASILON G30M 'Silicone'</b>
Density $\rho$ ( $\text{kg/m}^3$ ) <sup>b</sup>	957.1
Viscosity $\eta$ (Pa.s) <sup>b</sup>	$2.24 \times 10^4$
Power-law stress exponent <sup>b</sup>	0.996 (quasi-Newtonian)

<sup>a</sup> Rosenau et al., 2018; <sup>b</sup> Rudolf et al., 2016

## 166 **2.3 Scaling**

167 To achieve analogue models that are applicable to nature, an adequate geometric (length),  
168 kinematic (time) and dynamic (stress) scaling between model and nature must be established  
169 (Hubbert, 1937; Ramberg, 1981; Mulugeta, 1988; see also review by Schellart & Strak, 2016).  
170 For proper dynamic scaling and similarity in the brittle regime, the following equation, relating

171 material strength (here cohesion  $C$ ) and gravitational stresses (or overburden pressure), should  
172 be satisfied:

$$173 \quad C^* = \rho^* \times g^* \times l^* = \sigma^* \quad (1)$$

174 where  $C^*$ ,  $\rho^*$ ,  $g^*$ ,  $l^*$ , and  $\sigma^*$  are the model vs. nature ratios (called ‘scaling factors’) for cohesion,  
175 density, gravity, length, and stress respectively. Since the experiment is carried out under  
176 normal gravitational field in the laboratory,  $g^*$  is 1, and Eq. (1) reduces to:

$$177 \quad C^* = \rho^* \times l^* = \sigma^* \quad (2)$$

178 With setting up the model at laboratory scale we impose a geometric scaling factor (length ratio  
179  $l^*$ ) in the order of  $10^{-5}$  to  $10^{-6}$ , that is, 1 cm in the model represents c. 1 – 10 km in nature. The  
180 density ratio  $\rho^*$  is c. 0.7 (assuming an average density value to  $2400 \text{ kg/m}^3$  for sedimentary and  
181 crystalline rocks in the upper crust). Therefore, dynamic similarity (from Eq. 2) is achieved  
182 with a material satisfying a cohesion ratio ( $C^*$ ) that equals a stress ratio ( $\sigma^*$ ) of  $7 \times 10^{-6}$  to  $7 \times 10^{-7}$ .  
183 Accordingly, our quartz sand with an average cohesion of a few tens of Pascal will be able to  
184 simulate brittle crustal rocks with cohesion in the range of approximately 10 – 100 MPa. This  
185 range is well within the range of cohesion values for brittle crustal rocks (e.g., Schellart, 2000;  
186 Klinkmüller et al., 2016; Schellart & Strak, 2016 and references therein).

187 Given that our model is dominated by brittle deformation whose behavior is therefore not time-  
188 dependent (as it would be for viscous models) we are free to choose a suitable time scale from  
189 dimensional consideration according to the equation:

$$190 \quad T^* = \frac{l^*}{V^*} \quad (3)$$

191 where  $T^*$ ,  $l^*$ , and  $V^*$  are the model vs. nature ratios of time, length, and velocity, respectively.

192 We derive the scaling factor for time by solving eq. (3) for the following values: model “plate”

193 velocity = 1.8 cm/hr, nature velocity = 3 mm/yr (e.g. average extension rate for the East African  
194 Rift; Saria et al., 2014), and length scale as above. Accordingly, we arrive at a time scaling such  
195 that 1 hr in our model scales up to ca. 2 – 20 Ma in nature.

196 We note that even if we consider that our models are brittle-dominated and display time-  
197 independent behaviour, the rheology of the weak zone material needs consideration in the  
198 context of its viscous behavior, as the expected strain rate defines how weak the crust is in the  
199 weak zone region compared to the normal crust. The viscous strength of any flowing material  
200 is the viscosity times the strain rate. For a strain rate of  $10^{-5}$ /s as in our experiments (see  
201 appendix 2) it follows that the weak zone material strength is about 0.1 Pa, which is 100 to  
202 10,000 times lower than the strength of the quartz sand layer that increases linearly with depth  
203 from cohesion values near the surface to about 700-800 Pa at the base of the 4 cm thick models.  
204 Therefore, we consider the contribution of the weak zone itself to the integrated strength of the  
205 model crust to be negligible. The integrated model crustal strength (i.e. the area beneath the  
206 strength profile) in the area underlain by the weak zone is proportional to the squared thickness  
207 of the layer above the weak zone (see Zwaan et al., 2020, for a geometric derivation of this  
208 scaling). Accordingly, for 1 cm- and 2 cm- thick weak zones in an overall 4 cm thick layer  
209 model crust, the integrated strength in the weak zone area is reduced to ca. 56% and 25%  
210 respectively, of the integrated strength of the normal (pristine or sand-only) model crust.

## 211 **2.4 Model series design**

212 We present a reference model (R), and ten main models grouped into five main series (A – E;  
213 Table 2). The reference model consists of a 4 cm-thick sand layer (without a pre-extension weak  
214 zone) directly coupled to the extending foam. Series A and B focused on testing the extent to  
215 which the size (small vs large, respectively) and the orientation of pre-existing weak zones  
216 control the pattern of strain localization and partitioning in the overlying cover. In Series C, we

217 use the thickness of the overburden brittle-layer as a proxy to examine the influence of shallow  
218 vs. deep burial of pre-existing weak zones on the extent of strain localization in the overlying  
219 cover. Series D and E test the influence of the overall 3D geometry of pre-existing weak zones  
220 on deformation patterns during crustal extension. Details of the (i) orientation angle  $\theta$ , of the  
221 weak zone with respect to the applied extension direction, measured clockwise (positive angle)  
222 or anti-clockwise (negative angle) (ii) dimension and geometry of the weak zone, and (iii)  
223 integrated strength in the area underlain by the weak zone, with respect to the normal model  
224 crust, for each model are provided in Table 2. In this paper, models where the weak zone is  
225 orthogonal to the extension direction (i.e.,  $\theta = 90^\circ$ ) are referred to as *orthogonal extension*  
226 *models*, whereas those with oblique weak zone vs. extension direction angles (i.e.,  $\theta = 60^\circ$  and  
227  $45^\circ$ ) are referred to as *oblique extension models*. Note that in Series E model, the weak zone  
228 was curvilinear implying that about half of the weak zone is orthogonal to the extension  
229 direction ( $\theta = 90^\circ$ ) and half is oblique to the extension direction ( $\theta = 60^\circ$ ).

230 *Table 2: Summary of experimental series*

Experiment Series	Model Run	Brittle Layer (G12 Sand) Thickness (cm)	Weak zone (silicone)				Strain Analysis (presented in this paper)	
			Orientation, $\theta$ (w.r.t. extension direction)	Dimension/Size	Weakness (Integrated strength in weak zone area w.r.t. normal model crust)	Geometry/Shape	Normal strain $E_n$	Shear strain $E_s$
				<i>Small = 30 x 1 x 1 cm</i> <i>Large = 30 x 2 x 2 cm</i>				
Reference	Model R	4	-	-	-	-	X	X
Series A	Model A1	4	90°	Small	56%	Cuboid	X	X
	Model A2	4	60°	Small	56%	Cuboid	X	X
	Model A3	4	45°	Small	56%	Cuboid	X	X
Series B	Model B1	4	90°	Large	25%	Cuboid	X	X
	Model B2	4	60°	Large	25%	Cuboid	X	X
	Model B3	4	45°	Large	25%	Cuboid	X	X
Series C	Model C	1.5	45°	Small	44%	Cuboid	X	
Series D	Model D1	4	- 60°	See Fig. 2f	$\geq 56\%$	Triangular prism	X	
	Model D2	4	- 60°	See Fig. 2f	$\geq 56\%$	Semi-cylindrical	X	
Series E	Model E	4	Curvilinear (see text)	See Fig. 2f	$\geq 56\%$	Semi-cylindrical	X	

231

## 232 **2.5 Surface deformation monitoring**

233 We used a stereoscopic pair of two 12-bit, 29-megapixel monochrome CCD (charge-coupled  
234 device) cameras (LaVision Imager XLite 29M) mounted c. 1 m above the model surface with  
235 oblique viewing angles (Fig. 2d). Images were recorded at an image frequency of 0.05 Hz,  
236 corresponding to one image every 20 s, which, given the extension velocity (0.005 mm/s) of  
237 our models, represents one image per 0.1 mm of wall displacement.

238 To process the recorded images, we deployed a digital image correlation (DIC) technique, also  
239 known as particle imaging velocimetry (PIV), that allows us to monitor the surface deformation  
240 at high spatial and temporal resolution (e.g., White et al., 2001; Adam et al., 2005; Dautriat et  
241 al., 2011; Ge et al., 2019). We used commercial LaVision Davis 10 software employing a least-  
242 squares-method (LSM) to calculate the three-component deformation field between successive  
243 images. DIC processing was done at increments comparing every 10<sup>th</sup> image, representing 1  
244 mm of sidewall displacement. We find that this interval is not only computationally convenient,  
245 but also provides adequate information on the evolution of strain within our models at a high  
246 spatial and sufficient temporal resolution. To avoid the boundary effects, and further optimize  
247 computation time, DIC processing on the raw images was restricted to the central part of the  
248 model ('area of interest') by means of a rectangular mask (see Figs. 2b and 3).

249 The DIC results we present in this study are based on time-series of the 3D cumulative surface  
250 displacement field, where incremental displacements are summed up in a Lagrangian reference  
251 frame. From the 3D surface displacement field, the in-plane (2D horizontal) cumulative normal-  
252 ( $\epsilon_n$ ) and shear- ( $\epsilon_s$ ) strains were derived. The ability to decompose strain into normal and shear  
253 components highlight the key strength of the DIC analysis deployed in this study, in comparison  
254 to the numerous previous analogue models where deformation analysis has been mostly based  
255 on qualitative (rather than quantitative) visual inspection of model surface deformation at a

256 much lower spatial and temporal resolution. The computed strain distribution allows us to  
257 quantitatively assess the geometry and pattern of strain distribution of extension-related  
258 structures in our models at unprecedented resolution.

### 259 **3 Model Results**

260 The results are presented first in sections 3.1 – 3.4 based on the different experimental series.  
261 Within each section, we first present the final stage (c. 11% extension) of the model evolution  
262 by means of the surface fault pattern and the DIC-derived surface normal strain ( $\epsilon_n$ ). We also  
263 present the DIC-derived surface shear strain ( $\epsilon_s$ ) of the reference model, and Series A and B  
264 models, highlighting the oblique nature of first-order and secondary strike-slip structures. We  
265 finally provide cumulative model surface subsidence profiles illustrating the temporal evolution  
266 of topography. In section 3.5 we briefly highlight temporal aspects of structural evolution and  
267 in section 3.6 we quantify the obliquity of normal faulting in selected models. All data  
268 underlying this study and additional results of the DIC processing (not discussed here) are  
269 provided open access in Osagiede et al. (2020b).

#### 270 **3.1 Reference model R: Brittle-only (homogenous layer, no weak zone)**

271 The final stage (c. 11% extension) of the reference model surface is characterized by the  
272 occurrence of faults only along the boundaries of the model due to boundary effect resulting  
273 from the discontinuity between the sand layer and the model sidewalls (Fig. 3a). There is no  
274 localization of deformation in the central portion of the model. Instead, distributed, diffuse  
275 normal strain bands (c. 10% strain), orthogonal to the extension direction develop (Fig. 3b) with  
276 no associated shear strain (Fig. 3c). We interpret these diffuse strain bands as the equivalent of  
277 the distributed faulting reported in previous analogue models by both Schlagenhauf et al. (2008)  
278 and Zwaan et al. (2019). Diffuse strain plausibly a consequence of the larger grain size of the  
279 sand used in our setup (our mean grain size of 240  $\mu\text{m}$  vs. their c. 120  $\mu\text{m}$ ) and the higher

280 amount of extension applied in their models (our c. 11% vs. their  $\geq 13\%$ ). Apart from the diffuse  
281 strain bands, there is no significant shear strain localization in the model (Fig. 3c). The result  
282 of the reference model is important in this study because it allows us to differentiate the inherent  
283 model observations that are due to (i) the absence of a pre-existing weak zone and (ii) edge  
284 and/or basal boundary conditions associated with the overall model setup. The diffuse strain  
285 bands are interpreted to result from the distributed basal extension boundary condition (i.e.  
286 brittle layer directly on basal foam) in our model setup, and are not considered or interpreted  
287 further in this paper.

288 *Insert Figure 3*

### 289 **3.2 Experimental Series A and B: small- vs. large- sized weak zones with variable** 290 **orientation**

291 The model surface deformation after the final stage (c. 11%) extension of Models A1 (small  
292 weak zone,  $\theta = 90^\circ$ ), A2 (small weak zone,  $\theta = 60^\circ$ ), B1 (large weak zone,  $\theta = 90^\circ$ ), B2 (large  
293 weak zone,  $\theta = 60^\circ$ ) and B3 (large weak zone,  $\theta = 45^\circ$ ) are characterized by surface displacement  
294 along normal faults that bound model rift-related graben (herein referred to as graben-bounding  
295 faults) and which form directly above and parallel to the underlying weak zone (Figs. 4a, 4f,  
296 5a, 5f, and 5k). The graben-bounding faults are well constrained as localized, high normal strain  
297 zones ( $\geq 20\%$ , Figs. 4b, 4g, 5b, 5g, and 5l). The final stage of Model A3 (small weak zone,  $\theta =$   
298  $45^\circ$ ) differed to other models in that a rift-related graben structure did not develop (Fig. 4k and  
299 4l). This suggests that the weak zone in this model does not weaken the brittle layer sufficiently  
300 to allow for strain localization and surface displacement on graben-bounding faults under  
301 moderate obliquity.

302 In the orthogonal extension models (A1 and B1), the graben-bounding faults are through-going  
303 with an overall orientation that is perpendicular to the extension direction, except around the



304 fault tips where the fault geometry slightly deflects outward (Figs. 4a, 4b, 4d, 5a, 5b and 5d).  
305 The fault tip deflection is most likely a boundary effect that is due to both the transverse  
306 contraction (Poisson's effect) imposed by the basal foam, and the slope of the sand layer on the  
307 unconfined sides of the model-setup (Fig. 2a and 3). In Model B1, intra-graben faults that are  
308 parallel but antithetic to the main graben-bounding faults also develop, resulting in the  
309 formation of a central horst separating double marginal grabens (Figs. 5a, 5b and 5d). Similar  
310 deformation pattern where double marginal grabens develop have been previously described in  
311 numerous analogue studies (e.g., Allemand & Brun, 1991; Keep & McClay, 1997; Corti, 2004;  
312 Schreurs et al., 2006; Corti, 2012; Zwaan et al., 2019). In the oblique extension models (A2,  
313 B2, and B3), the resulting graben-bounding faults are generally oblique to the extension  
314 direction, except at the lateral tips of the faults where their geometry deflects, becoming near-  
315 orthogonal to the extension direction (Figs. 4f, 4g, 4i, 5f, 5g, 5i, 5k, 5l and 5n). The normal  
316 strain component shows that in some of the models, specifically Models B1 and B2, there are  
317 ellipsoidal-shaped zones of approximately zero-strain (little or no deformation) in the  
318 immediate footwall and/or hangingwall of the graben-bounding faults (blue zones in Figs. 5b  
319 and 5g). These zones are here referred to as strain shadows (Figs. 5d and 5i) (e.g., Ackermann  
320 & Schlische, 1997; Cowie, 1998; Gupta & Scholz, 2000; Soliva et al., 2006; Deng et al., 2017).

321

*Insert Figure 4*

322

*Insert Figure 5*

323 The shear strain component of the deformation provides insight into the role of oblique slip and  
324 strike-slip during rift evolution, particularly under oblique extension (Withjack & Jamison,  
325 1986). In the orthogonal extension models (Models A1 and B1), the pattern of the shear strain  
326 distribution along the graben-bounding faults is largely chaotic in the central part of the faults,  
327 and more systematic only at the fault tips (Figs. 4c and 5c). The chaotic shear strain pattern  
328 reflects pure-dip slip in the central part of the graben-bounding faults. Some systematic oblique  
329 slip is indicated at the fault tips which is consistent with lateral contraction imposed on the  
330 model by the basal foam. Within the graben (especially Model A1), there are poorly developed,  
331 diffuse shear strain zones ( $c. \pm 0.3\%$ ). These were not obvious in the normal strain pattern  
332 indicating their pure strike-slip nature. We interpret these as sets of conjugate strike-slip faults  
333 formed in response to the small lateral contraction imposed by the basal foam in an overall pure  
334 shear regime (see Appendix 3). These poorly developed conjugate shears within the graben are  
335 typically not observed in natural rifts, and thus are considered here as basal boundary effects,  
336 and are not considered further in this paper.

337 In oblique extension models A2, B2 and B3, the overall shear strain distribution is generally  
338 similar and consistent with strain partitioning in transtensional kinematics (see Appendix 3).  
339 The graben-bounding faults are consequently characterized by a minor component of dextral  
340 shear motion (Figs. 4h, 5h and 5m). Within the graben, en échelon, sigmoidal zones of sinistral  
341 (i.e. antithetic) shear developed (especially in Models A2 and B3). These intra-graben structures  
342 did not accommodate vertical surface displacement as they are not apparent in the normal strain  
343 component of the model deformation, indicating that they are purely strike-slip structures. We  
344 interpret them as antithetic Riedel (R') shears related to the simple shear component of

345 transtension. These R' shears are even seen in Model A3 (Fig. 4m), although no main graben  
346 developed as observed from the model surface and normal strain analysis (see Figs. 4k and 4l).  
347 The overall en échelon arrangement of the R' shears is parallel to the underlying weak zone,  
348 whereas the individual R' shears are near-orthogonal to the extension direction.

349 The width of the rift-graben is approximately the same (c. 4cm) for Models A1 and B1,  
350 irrespective of the size of the underlying weak zone (compare Figs. 4a and 5a), whereas it is  
351 slightly narrower with decreasing  $\theta$ -angle (compare Figs. 5a, 5f and 5k). The width of the rift-  
352 graben is unaffected by the size of the weak zone because the graben width is not only  
353 dependent on the thickness of the brittle layer above the weak zone and the dip of the graben-  
354 bounding faults, but also on the width of the weak zone (Corti, 2004) (see Appendix 4). Time-  
355 series cross-sectional profiles of the models show that the subsidence is symmetric within the  
356 rift-graben (Figs. 4e, 4j, 5e, 5j and 5o), except for Model A3 where the profiles are flat because  
357 no graben developed in the model (Fig. 4o). Whereas the model surface outside the model rift-  
358 graben generally subsides at rather constant rates (equidistant horizontal profile segments)  
359 consistent with distributed thinning, the rift-graben floors show indications of variable  
360 subsidence rates over the model run. The absolute degree of subsidence varies between models,  
361 generally increasing with increasing size of the underlying weak zone (compare Figs. 4e and  
362 5e) and decreasing with decreasing  $\theta$ -angle (compare Figs. 5e, 5j and 5o). The subsidence rate  
363 is positively correlated to the amount of vertical displacement accommodated by the graben-  
364 bounding faults. Interestingly, the subsidence profile also show zones of relative footwall uplift  
365 with magnitudes that positively correlate with amount of vertical displacement of the associated  
366 graben-bounding faults (Figs. 4e, 5e, 5j).

### 367 **3.3 Experimental Series C: thin brittle layer**

368 We here compare an additional model (Model C) where the thickness of the brittle layer was  
369 reduced to 1.5 cm with Series A models that had 4 cm-thick brittle layers. Model C has a small  
370 (1 cm-thick) weak zone that is oriented  $\theta = 45^\circ$ . The only difference between the setup of Model  
371 C and A3 is the thickness of the brittle layer. Thus, the brittle layer thickness above the weak  
372 zone is 0.5 cm and 3 cm for Model C and A3, respectively. In the final stage of extension,  
373 Model C is characterized by surface displacement and strain localization along graben-  
374 bounding faults that form directly above and parallel to the underlying weak zone (Figs. 6a–c).  
375 This observation provides insight on the effect of the depth of the weak zone, since Model A3  
376 with a thicker overburden brittle layer did not localize deformation (compare Figs. 6a and 4k).  
377 The graben structure in Model C is c. 1 cm and narrower than those formed in Series A.  
378 Furthermore, the normal strain distribution along the graben-bounding faults is characterized  
379 by several local maxima (Figs. 6b–c). The location of these strain maxima coincides with the  
380 termination zone of the diffuse strain bands on the obliquely oriented graben-bounding faults,  
381 and thus could be considered a boundary effect. Time-series cross-sectional profiles of the  
382 model show that the subsidence is symmetric within the rift-graben (Fig. 6d).

383 *Insert Figure 6*

### 384 **3.4 Experimental Series D and E: variable weak zone geometry**

385 Figure 8 shows the results of the final stage (c. 11%) extension of three models (Models D1,  
386 D2, and E) with different weak zone geometries, simulating a range of cross-sectional and plan-  
387 view geometries that pre-existing weak zones may exhibit in nature. Overall, the deformation  
388 patterns of these models are more complex compared to the models in Series A – C, in which  
389 we used geometrically simple, cuboid-shaped weak zones.

390 In Model D1 with an upward pointing triangular prism-shaped weak zone, the normal strain  
391 distribution across the graben structure is quite asymmetrical (Figs. 7a–b). The ‘southern’  
392 boundary of the graben is characterized by a through-going border fault, with a zig-zag  
393 geometry consisting of relatively longer segments that are parallel to the underlying weak zone,  
394 and shorter jogs that are subparallel to the extension direction (Fig. 7c). The zig-zag geometry  
395 reflects growth by the (at-surface) linkage of initially isolated weak zone-parallel fault  
396 segments. However, the strain distribution pattern along the ‘northern’ boundary of the graben  
397 is more complex. Unlike the southern boundary, the northern boundary is characterized by a  
398 wider zone of faulting, with a dominant right-stepping en échelon faulting style (Figs.  
399 7a–c). The en echelon fault set consists of individual fault segments which are oriented sub-  
400 perpendicular to the extension direction but is overall aligned parallel to the underlying weak  
401 zone. Time-series cross-sectional profiles show asymmetric subsidence within the rift-graben,  
402 broadly reflecting a half-graben structure (Fig. 7d).

403 *Insert Figure 7*

404 In Model D2 with a broader, deformed semi-cylindrical-shaped weak zone, normal strain  
405 distribution on the borders of the graben structure is near-symmetrical (Figs. 7e–f). This differs  
406 from the asymmetric strain distribution observed in Model D1. In contrast to the discrete  
407 graben-bounding faults observed in Series A – C models, the graben in Model D2 is bounded  
408 relatively wide (c. 2.5 cm) deformation (fault) zones on both margins (Figs. 7e–f). The wide  
409 fault zones are characterized by variable fault styles, including; subparallel fault sets,  
410 anastomosing faults (*sensu* Peacock et al., 2016), and right-stepping en échelon faults (within  
411 the ‘northern’ border fault zone, similar to Model C8) (Fig. 7g). Within the graben, discrete  
412 intra-graben fault develops parallel to the underlying weak zone. The intra-graben fault  
413 accumulates higher amount of deformation (c.  $\geq 20\%$  strain) compared to the border fault zone

414 (Fig. 7f). The time-series cross-sectional profiles of the graben subsidence is symmetrical,  
415 unlike that of Model D1 (Fig. 7h). Also, the symmetry of the subsidence profile is characterized  
416 by a ‘dual slope’ and differs from the ‘single slope’ symmetry of Series A – C models (compare  
417 Fig. 7h with profiles in Figs. 4, 5, and 6).

418 Model E contains a weak zone that has a deformed semi-circular cross section, but curvilinear  
419 planform geometry. The normal strain distribution is similar to Model D2, with wide (c. 2.5  
420 cm) fault zones bounding the rift-graben structure (Figs. 7i–j). The wide fault zones also exhibit  
421 variable fault styles (Fig. 7k). Like Model D2, the intra-graben fault is parallel to the underlying  
422 weak zone, and accumulates higher amount of deformation compared to the border fault zone  
423 (Fig. 7j). However, the development of the intra-graben fault is only limited to the eastern  
424 portion of the graben structure that is oblique to the extension direction, and do not extend to,  
425 or develop in, the western portion that is perpendicular to the extension direction. The time-  
426 series cross-sectional profiles of the graben subsidence is symmetrical, and identical to that of  
427 Model D2 (Fig. 7l).

### 428 **3.5 Temporal evolution of model structures**

429 To illustrate the temporal evolution of the model structures, we briefly present the early  
430 (extension = 2.2%), intermediate (extension = 6.7%), and final (extension = 11.1%) stages of  
431 normal strain evolution of some Series A and B models (Fig. 8). The timing of faulting and  
432 amount of strain accommodated by the faults varies in these models. For example, whereas the  
433 graben-bounding faults in Model A1 (small weak zone,  $\theta = 90^\circ$ ) accommodated only c. 5%  
434 strain at the early stage of extension, its equivalent in Model B1 (large weak zone,  $\theta = 90^\circ$ )  
435 already accommodated up to 15% strain by the same stage (compare Figs. 8a and c). Similarly,  
436 the graben-bounding faults in Model B2 (large weak zone,  $\theta = 60^\circ$ ) accommodated more strain  
437 than in Model A2 (small weak zone,  $\theta = 60^\circ$ ) at the same stages (compare Figs. 8b and d).

438 Furthermore, Comparing Models A1 and A2 show that whereas graben-bounding faults  
439 initiated early (during the early stage) as through-going faults in Model A1, they initiated later  
440 as mostly isolated, en échelon faults in Model A2 (compare Figs. 8a and b). The en échelon  
441 faults are left-stepping and aligned parallel to the underlying pre-existing weak zone (Fig. 8b).  
442 There is a two-phase sequential evolution of the rift-related faults in Model B1. The first phase  
443 is characterized by the initiation and accumulation of normal strain (vertical displacement) on  
444 the graben-bounding faults during the early stage of the model deformation, and the second  
445 phase is characterized by the initiation and accumulation of normal strain on antithetic intra-  
446 graben faults during the intermediate – late stage (Fig. 8c). A similar, but less-well developed  
447 two-phase development of the faults is also observed in Model B2 (Fig. 8d).

448 *Insert Figure 8*

### 449 **3.6 Quantifying the normal vs. shear strain on model structures**

450 To quantify the obliqueness of normal faults we analyse the relative amount of normal vs shear  
451 components of strain accommodated by the graben-bounding faults and discrete intra-graben  
452 faults (when formed). The finite normal and shear strain are plotted along profiles that are  
453 parallel to the model extension direction (Fig. 9). The plots highlight the overall style of the  
454 graben-bounding faults, consisting mainly of either narrow (single) border faults (Models A1,  
455 A2, B1, B2, B3, and C), wide border fault zones (Models D2 and E), or both (Model D1) (Fig.  
456 9). In Model A3, both the normal and shear strain lines are flat because strain did not localize  
457 in the model domain (Fig. 9i). These styles are consistent with the observations from the model  
458 surface and strain maps of the respective models (Figs. 4, 5, 6, and 7).

459 In the orthogonal extension models (Models A1, B1, and the orthogonal half of Model E), the  
460 strain accommodated by the graben-bounding and intra-graben faults is 100% normal strain and

461 zero shear strain consistent with pure normal faulting (Figs. 9a–c). In the oblique extension  
462 models (Models A2, B2, B3, C, D1, D2, and the oblique half of Model E), the strain  
463 accommodated by the graben-bounding and intra-graben faults compose of both normal and  
464 shear components with a variable relative ratio between the models (Figs. 9d–h, j–k). In Model  
465 A2, the finite normal strain on the graben-bounding fault is c. 0.11, whereas the shear strain is  
466 c. 0.01, implying that the shear strain is approximately one-tenth of the total strain on the fault  
467 (Fig. 9e). For Model B2, normal strain is c. 0.4, and shear strain is c. 0.1, implying that the shear  
468 strain is approximately one-fifth of the total strain on the fault (Fig. 9f). For Model B3, normal  
469 strain is c. 0.19, and shear strain is c. 0.06, implying that the shear strain is approximately one-  
470 fourth of the total strain on the fault (Fig. 9j). For Model C, the values of normal and shear  
471 strain are approximately the same as in Model B3, and shear strain is about one-fourth of the  
472 total strain on the fault (Fig. 9k). For Model D1, normal strain on the narrow border fault is c.  
473 0.26, and shear strain is c. 0.06, implying that the shear strain is approximately one-fifth of the  
474 total strain on the fault (Fig. 9g). For Model D2, average normal strain on the wide border fault  
475 zone is c. 0.15, and average shear strain is c. 0.04, implying that the shear strain is approximately  
476 one-fifth of the total strain on the fault (Fig. 9h). Normal strain on the intra-graben fault is c.  
477 0.27, and shear strain is c. 0.18, implying that the shear strain is approximately two-fifth of the  
478 total strain on the fault (Fig. 9h). For the oblique ( $\theta = -60^\circ$ ) half of Model E, the normal and  
479 shear strain patterns are identical to Model D2, underpinning the reproducibility of the models  
480 (compare Figs. 9d and h). Consequently, the normal and shear strain on the wide border fault  
481 zone and intra-graben fault in Model E and D2 are similar.

482 *Insert Figure 9*

483 In summary, in the orthogonal extension models, shear strain does not contribute to the total  
484 strain accommodated by the graben-bounding and intra-graben faults, except at the fault tips as



485 observed in the strain maps described earlier (see Figs. 4c and 5c). These faults are orthogonal  
486 to the extension direction. In the oblique extension models, when  $\theta = \pm 60^\circ$  (low obliquity),  
487 shear strain account for only c. 20% (one-fifth) of the total strain accommodated by the graben-  
488 bounding faults and 40% (two-fifth) of the total strain accommodated by the intra-graben fault.  
489 When  $\theta = 45^\circ$  (moderate obliquity), the amount of shear strain on the graben-bounding faults  
490 increases to c. 25% (one-fourth) of the total strain.

## 491 **4 Discussion**

### 492 **4.1 Comparison with previous analogue and numerical modeling studies**

493 Observations from our models are broadly consistent with previous studies. Here, we briefly  
494 compare our key observations with observations from previous modeling studies and highlight  
495 the similarities and differences, where applicable.

496 First, the varying influence of a pre-existing crustal weak zone because of its orientation or  
497 depth compares well with previous models. For example, the ability of a weak zone to localize  
498 deformation is strongly influenced by the orientation of the crustal weak zone with respect to  
499 the model-extension direction, i.e., it localizes more when it is orthogonal (i.e., optimally  
500 oriented) and less with increasing obliquity (e.g., analytical solution by Ranalli & Yin, 1990;  
501 and analogue models by Zwaan & Schreurs, 2017; Molnar et al., 2019; Zwaan et al., in review).

502 Also, our observation that a shallow weak zone (thin crustal cover) localizes more strain than a  
503 deeper weak zone agrees with previous analogue model results by Sokoutis et al. (2007). The  
504 observation from our model on the effect of the depth of the weak zone on the width of the rift-  
505 graben is comparable to that of Dyksterhuis et al. (2007). That is, a shallower weak zone results  
506 in a narrower graben width. This is because a shallow weak zone reduces the effective thickness  
507 of the brittle layer above the weak zone (e.g., Allemand & Brun, 1991; Brun, 1999; Dyksterhuis  
508 et al., 2007). This is in line with predictions from mechanical models which suggest that the

509 width of a rift graben decreases with decreasing effective elastic thickness of the crust (Scholz  
510 & Contreras, 1998). The observation that the graben width narrows due to decreasing  $\theta$ -angle  
511 (increasing obliquity) of the weak zone agrees with previous analogue modeling studies (e.g.,  
512 Tron & Brun, 1991; Clifton et al., 2000; Zwaan et al., 2016). This is plausibly due to the  
513 increasing steepness/dip of the graben-border faults as they accommodate oblique-slip (e.g.,  
514 Tron & Brun, 1991; Zwaan et al., 2016).

515 Second, the two-phase temporal evolution of rift-related faults (early graben-bounding faults  
516 vs. late intra-graben structures) in our models compares well with the early boundary faults and  
517 later internal faults observed in the orthogonal and low to moderate oblique rift analogue models  
518 of Agostini et al. (2009). This reflects the progressive migration of strain from the borders of  
519 the rift-graben towards the center of the graben (Agostini et al., 2009). However, in our models,  
520 the intra-graben (internal) faults are less-well developed and thus generally poorly expressed in  
521 the model surface (e.g., Figs. 5a and f) compared to those generated by Agostini et al. (2009)  
522 and Philippon et al. (2015). This difference is likely due to a combination of factors including,  
523 (i) the difference in the model setup and boundary conditions (e.g., brittle-ductile in their  
524 models vs. brittle-only in our model), (ii) the intrinsic strain-localization properties of the brittle  
525 material (coarse quartz sand in our model vs. fine-grained K-feldspar powder in their models),  
526 and (iii) the amount of applied extension (c. 11% in our model vs. approximately double in their  
527 models).

528 Third, the partitioning of deformation (in terms of both fault orientation and sense of fault slip)  
529 between the border faults and intra-graben structures under our low ( $\theta = 60^\circ$ ) and moderately  
530 ( $\theta = 45^\circ$ ) oblique extension is consistent with several previous models. In terms of fault  
531 orientation, the graben-bounding faults are oriented obliquely to the extension direction,  
532 whereas the intra-graben structures (consisting of en échelon R' shears) are approximately

533 orthogonal to the extension direction. Such variability in the orientation of the border- vs.  
534 internal- structures have been observed in many previous low to moderate oblique-rifts  
535 analogue models (e.g., Withjack & Jamison, 1986; Tron & Brun, 1991; McClay & White, 1995;  
536 Bonini et al., 1997; Corti, 2008; Agostini et al., 2009; Autin et al., 2010; Philippon et al., 2015;  
537 Zwaan et al., 2016; Sani et al., 2019).

538 In terms of the sense of slip, an advantage of the high resolution DIC technique we deploy is  
539 that it allows even low strains (not captured by visual inspection) to be quantitatively  
540 decomposed into the normal- and shear- components based on the 3D displacement field. Thus,  
541 both the normal and shear sense of slip on the border- and internal- structures are constrained  
542 in our oblique extension models (Figs. 4, 5, and 9). Our data show that the border faults are  
543 oblique to the extension direction, and accommodate a major (80 – 75%) normal- and minor  
544 (20 – 25%) shear- components of strain, indicating they are oblique-slip faults, rather than pure  
545 dip-slip. Similar oblique-slip sense on faults striking oblique to the extension direction has been  
546 interpreted qualitatively in previous analogue models (e.g., Withjack & Jamison, 1986; Tron &  
547 Brun, 1991; Corti et al., 2007; Agostini et al., 2009; Corti, 2012; Molnar et al., 2019; Ghosh et  
548 al., 2020). Surprisingly, the extension-orthogonal, en échelon internal structures in our oblique  
549 extension models are pure strike-slip, differing from the dip-slip (vertical displacement)  
550 interpreted in earlier analogue (e.g., Corti, 2008; Agostini et al., 2009; Philippon et al., 2015)  
551 and numerical models (e.g., Brune, 2014; Duclaux et al., 2020). This difference can again  
552 possibly be explained by the difference in the amount of applied extension, which is comparably  
553 small (about half) in our study. For example, Agostini et al. (2009) showed that at low to  
554 moderate obliquity, the internal-rift faults only started accommodating vertical displacement  
555 and thus detectable surface expression after c. 12.5% of extension, which is higher than the total  
556 extension in our models. Similar oriented en-échelon internal structures but interpreted as  
557 normal faults are detected in numerical simulations at about 4% (Duclaux et al., 2020) to 20%

558 (Brune, 2014) extension. Duclaux et al. (2020) describe rotation of these structures in a  
559 synthetic sense with respect to the overall transtensional shear sense which would imply these  
560 normal faults have an antithetic strike-slip component as seen in our analogue models. The  
561 simulations of Brune (2014) suggest a set of strike-slip faults, where one is sub-parallel to the  
562 normal faults and one more oblique. We here infer that the internal structures possibly initiate  
563 as pure strike-slip (R' shear) structures (largely invisible to traditional monitoring techniques),  
564 which will later rotate and evolve to mainly dip-slip faults as extension increases (c. >10%  
565 extension) and strain migrates to the center of the rift-graben. It is however noteworthy that  
566 material properties controlling strain localization (i.e. strain weakening parameters) may  
567 significantly differ between nature, analog and numerical models and thus the evolution may  
568 only qualitatively follow the here suggested path. In any case, the application of the DIC  
569 technique in our analogue models thus provides new insights into the early-stage development  
570 of these internal rift structures that are not resolvable in previous analogue modeling studies  
571 using traditional visual inspection (e.g., Agostini et al., 2009; Philippon et al., 2015).

572 Lastly, the along-strike slip variation that characterizes the extension-orthogonal graben-  
573 bounding faults in our orthogonal extension models, i.e., pure dip-slip at the center of the faults  
574 and opposing sense of oblique-slip at the fault tips resemble observations from previous  
575 analogue- (Corti et al., 2013; Philippon et al., 2015) and numerical- (Maniatis & Hampel, 2008)  
576 models. However, in the previous models the opposing sense of oblique-slip kinematics at the  
577 fault tips converges towards the center of the individual faults (see Philippon et al., 2015),  
578 whereas in our model, it diverges away from the fault center (Figs. 4d and 5d). While  
579 convergent slip along single faults can be understood in terms of stretching with volume  
580 conservation (i.e. Poisson effect), divergent slip as observed in our models is interpreted as a  
581 boundary effect. More specifically, this likely relates to the inward drag of the deforming  
582 footwall block because of its direct frictional coupling to the laterally shortening basal foam

583 while the hangingwall block, underlain by silicone, is decoupled from the foam and behaves  
584 like a more rigid block, resisting lateral shortening.

#### 585 **4.2 Controls on strain localization above pre-existing weak zones in natural rift systems**

586 Our models provide insights into the way in which pre-existing weak zones may influence the  
587 structural style and drive strain localization during extension. During extension, the presence  
588 of an underlying pre-existing weak zone results in the development and localization of strain  
589 on graben-bounding faults and fault zones that form in the brittle cover, in all but one of the  
590 simulated scenarios (Model A3) (Figs. 4, 5, 6, and 7).

591 In experimental Series A and B, in which the size and orientation of the weak zone were varied,  
592 we observe that strain preferentially localized on graben-bounding faults in the brittle cover  
593 when the weak zone is oriented at  $\geq 60^\circ$  to the extension direction, irrespective of the size of  
594 the weak zone (Figs. 4a–j and 5a–j). When the weak zone is oriented  $45^\circ$  to the extension  
595 direction, the presence of the large weak zone (Model B3) resulted in strain localization along  
596 graben-bounding faults, whereas the small weak zone (Model A3) did not (Figs. 4k and 5k).  
597 This suggests that the control exerted by the size of pre-existing weak zones becomes  
598 increasingly more important with increasing obliquity of the weak zone with respect to the  
599 regional maximum extension direction. As the angle between the orientations of pre-existing  
600 weak zone and the extension direction reduces ( $\theta \leq 45^\circ$ ), smaller-scale weak zones are less  
601 likely to locally perturb the regional stress field and localize strain, whereas, larger-scale weak  
602 zones may still localize strain at a much lower angle of orientation with respect to the extension  
603 direction. Ranalli and Yin (1990) presented detailed analytical solutions that demonstrates that  
604 the critical differential stress ( $\sigma_1 - \sigma_3$ ) required for strain localization and eventual faulting on  
605 a plane parallel to a pre-existing strength anisotropy (i.e. weak zone) is dependent on: (1) the  
606 material parameters and layering, which controls the yield stress curve/strength profile, and the

607 integrated strength in the vicinity of the anisotropy, compared to that of the homogenous,  
608 pristine column of the simulated crust (as quantified in Table 2, see also Fig. 2e), and (2) the  
609 orientation of the strength anisotropy, that is, there is a maximum orientation with respect to  
610 the principal extension direction (as a function of the integrated strength), beyond which strain  
611 localization is no longer possible along the anisotropy.

612 Comparing the results of Model A3 and Model C provides insight on the possible role of the  
613 depth of pre-existing weak zones on normal fault evolution, since the size (small) and  
614 orientation ( $\theta = 45^\circ$ ) of the weak zone are the same, but Model C has a thinner brittle layer. In  
615 contrast to the lack of graben-bounding faults in the model with the thicker brittle layer (Model  
616 A3; Figs. 4k–o), strain localization on graben-bounding faults occurs above the weak zone in  
617 the thinner brittle layer (Model C; Figs. 6a–d). This suggests that a shallow pre-existing weak  
618 zone is more likely to localize strain in the brittle cover compared to a deep weak zone. Again,  
619 this is in strong agreement with Ranalli and Yin (1990), where they showed that critical  
620 differential stress increases with depth, implying that a lesser critical differential stress is  
621 required for strain to localize in the vicinity of shallow weak zones compared to deeper weak  
622 zones.

623 Our model observations correlate well with observations in many natural rifts such as the  
624 northern North Sea Rift (e.g., Phillips et al., 2016; Phillips et al., 2019; Osagiede et al., 2020a),  
625 Taranaki Basin, New Zealand (Collanega et al., 2019), and East African Rift (e.g., Daly et al.,  
626 1989; Morley, 1995), where some underlying pre-existing shear zones influenced the location,  
627 segmentation, and geometry of subsequent rift-related structures, whereas others had limited or  
628 no influence. For example, to the south of the western branch of the East African Rift System,  
629 the Rukwa-Malawi Rift segments preferentially developed along the large-scale NW-SE-  
630 trending inter-cratonic Ubendian mobile belt consisting of amalgamated Precambrian shear

631 zones, whereas the N-S-trending Kenya Rift cross-cut the similar, but smaller-scale NW-SE-  
632 trending Aswa Shear Zone (see Fig. 1d) (e.g., Daly et al., 1989; Morley, 1995; Theunissen et  
633 al., 1996). More specifically, our work suggests that this selective influence of pre-existing  
634 weak zones on strain localization during extension is controlled by a complex interplay between  
635 the orientation, size, and depth of occurrence of the weak zones (Fig. 10). This conclusion  
636 supports previous suggestion by Phillips et al. (2016) where only 1-2 km thick (and not thin c.  
637 100 m) Devonian shear zones preferentially reactivated and influenced younger rift faults in the  
638 northern North Sea. Similarly, Osagiede et al. (2020a) report that the Utsira Shear Zone (with  
639 a thickness  $> 3$  km) locally perturbed the regional stress field during the Middle Jurassic – Early  
640 Cretaceous rift phase in the northern North Sea, thus influencing the geometry and growth of  
641 the cover rift faults, whereas the Heimdal Shear Zone ( $< 1$  km-thick) had no influence on cover  
642 faults (see Fig. 1b).

643 *Insert Figure 10*

644 **4.3. Influence of pre-existing weak zones on overall rift architecture**

645 **4.3.1 Influence on the development and timing of rift structures**

646 In the models in which the underlying weak zone induces strain localization, the resulting  
647 graben is broadly parallel to the weak zone. However, the graben-bounding faults exhibits a  
648 range of styles from discrete through-going border faults that mimic the orientation of the weak  
649 zone (especially in orthogonal extension models), to individual en échelon fault segments that  
650 may be oblique to the weak zone (in some oblique extension models) (compare Figs. 8a and b).  
651 En échelon faults are characteristic of oblique extension and are observed in several oblique rift  
652 modeling studies (Withjack & Jamison, 1986; Tron & Brun, 1991; McClay & White, 1995;  
653 Clifton et al., 2000; Van Wijk, 2005; Agostini et al., 2009; Zwaan et al., in review). Overall,  
654 the correlation between the location, segmentation and orientation of the graben-bounding

655 faults and the underlying weak zone indicates that the growth and geometry of the rift normal  
656 faults was strongly influenced by the weak zone (e.g., Collanega et al., 2019; Osagiede et al.,  
657 2020a).

658 Our quantitative model results provide new insights into how pre-existing weak zones control  
659 the timing of fault development in rifts. We find differences in the timing of faulting and the  
660 amount of strain accommodated by graben-bounding faults, as a function of either the  
661 orientation, size, or the depth of the weak zone. Graben-bounding faults nucleate earlier and  
662 accommodate more normal strain in orthogonal extension models compared to oblique  
663 extension models, where a complementary part of the strain is accommodated by oblique slip  
664 and intra-graben strike-slip (cf. Model A1 and A2; Figs. 8, 9). For models with the same weak  
665 zone orientation, the graben-bounding faults nucleate earlier for the thicker and/or shallower  
666 weak zone and accumulate more strain causing more pronounced strain shadows (cf. Model A2  
667 and B2; Figs. 8b and d, 5g).

#### 668 **4.3.2 Influence on the style of bounding fault system**

669 We observe that the 3D geometry of the underlying weak zone dictates whether strain localizes  
670 on either (i) narrow, discrete faults, or (ii) wide, diffuse fault zones, which ultimately bound  
671 rift-related graben. In many natural rift systems, for example the North Sea, pre-existing weak  
672 zones (e.g. ductile shear zones) exhibit a range of map-view geometries, from largely linear  
673 (e.g., Hardangerfjord Shear Zone) to curvilinear (e.g., Utsira Shear Zone) (Fig. 1a). In this  
674 study, we did not attempt to directly simulate any specific natural 3D weak zone geometry due  
675 to the complexity of these geometries in nature. However, we used four simplified, generic  
676 weak zone geometries in our models (see Table 2 and Fig. 2f). All models in Experimental  
677 Series A, B and C, where rift graben developed, were characterized by near-symmetrical strain  
678 localization on very narrow zones at the margins of the graben, resulting in a single or



679 segmented border faults (Fig. 4, 5, 6, and 9). In all these models, the same weak zone geometry  
680 that simulates a block-like weak zone was used, and thus provides evidence of a striking  
681 relationship between the geometry of the weak zone and the distribution of strain.

682 Conversely, in Experimental Series D and E where we used weak zone geometries that  
683 simulated anticlinal weak zones, strain at the graben margins was more diffuse, resulting in a  
684 more structurally complex rift architecture characterized by the development of fault zones (and  
685 not a single-fault) on both margins (Fig. 7 and 9). These fault zones are characterized by a range  
686 of fault styles, including, near-parallel-, en échelon-, and anastomosing fault sets. Furthermore,  
687 the observed differences in the strain distribution in experimental Series D and E appears to  
688 also be related to whether the anticlinal geometry is ‘tight’ (Model D1), or ‘gentle’ (Models D2  
689 and E) (Fig. 7). These results suggest that rift architecture is at least partly controlled by the 3D  
690 geometry of the pre-existing weakness.

#### 691 **4.3.3 Influence on strain partitioning under oblique extension**

692 We have also observed significant strain partitioning in the oblique extension models,  
693 suggesting that oblique-slip and strike-slip are important mechanisms in the development of  
694 oblique rifts (e.g., Figs. 4h and 5m). A well-documented example is the NW-SE-trending Gulf  
695 of California, Mexico. Withjack and Jamison (1986) compared the pattern of faulting and strain  
696 partitioning in their analogue and analytical models to observations of a second rifting episode  
697 characterized by both normal to oblique-slip, and strike-slip faulting in the Gulf of California.  
698 Based on this comparison, they inferred that the pattern of faulting and strain partitioning  
699 observed in the Gulf of California best fits with an oblique rift system where the rift trend is c.  
700 30° to the relative displacement direction. The Gulf of California is therefore a highly oblique  
701 rift system where fault slip data show that E-W extension is accommodated by both oblique-

702 slip (majorly dip-slip with minor dextral component) dominating the rift margin faults, and  
703 strike-slip dominating the intra-Gulf domain (see Bonini et al., 2019).

704 Our observations of oblique slip on graben-bounding faults in our oblique extension models  
705 imply that in extensional settings, normal faults that are oblique to the regional extension  
706 direction most likely accommodates deformation by both dip- and strike- slip displacements.  
707 Although the dip-slip component of such faults may be greater, they are, however, not pure  
708 normal faults, but rather oblique normal faults. This is the case in the border faults of the NE-  
709 trending rift graben of the Parnaíba Basin, Brazil, which developed as a result of the reactivation  
710 of the underlying NE-SW-trending Transbrasiliano Shear Zone under N-S regional extension  
711 (Fig. 1c) (see de Castro et al., 2016). Similar minor strike-slip component is reported in several  
712 border fault systems that are oblique to the regional extension direction in other natural rift  
713 settings, including the Northern Main Ethiopian Rift (e.g., Boccaletti et al., 1998; Corti, 2009),  
714 Gulf of Aden (Dauteuil et al., 2001), the Gulf of California (e.g., Withjack & Jamison, 1986;  
715 Bonini et al., 2019), and the Mohns Ridge, Norwegian Sea (Dauteuil & Brun, 1996). We note  
716 that, in outcrop-based fault analysis, the horizontal offset of markers and kinematic indicators  
717 such as slickenlines allows for the discrimination of oblique normal faults from pure normal  
718 faults. However, in seismic reflection-based analysis, it is more challenging to constrain the  
719 strike-slip component of displacement on normal faults due to the absence of obvious kinematic  
720 indicators, and as such only the dip-slip (throw) component is quantified. Therefore, care should  
721 be taken when using results of such analysis to scale fault length – displacement relationship,  
722 as they may likely skew such relationship more towards under displaced faults.

723 In contrast to settings where faults that are oblique to the regional extension direction  
724 accommodate deformation by both dip- and strike- slip displacements, other natural examples  
725 have been observed where faults striking oblique to the regional extension are pure dip-slip

726 (normal) faults, e.g., the Rukwa Rift segment of the East African Rift (Morley, 2010), and Main  
727 Ethiopian Rift (Corti et al., 2013). To explain the later, Morley (2010) proposed that the  
728 presence of pre-existing weak zones in the brittle crust can result in the local re-orientation of  
729 the regional stress field, such that the maximum horizontal stress lies sub-parallel to the weak  
730 zone. This explanation has been supported by the interpretation of analogue models by Corti et  
731 al. (2013) and Philippon et al. (2015) partly based on re-analysis of earlier analogue models.  
732 This contrasting influence of pre-existing weak zones raises an important question of which  
733 conditions favor strain partitioning vs. stress re-orientation in extensional settings. Although  
734 answering this question is beyond the scope of this current study, we note that Philippon and  
735 Corti (2016) suggested that a moderate obliquity threshold of  $45^\circ$  could mark the transition from  
736 stress re-orientation to strain partitioning in a divergent setting, while our model results suggests  
737 that strain partitioning may already occur at lower obliquity. The difference could lie in the  
738 different experimental methods used (centrifuge vs. normal gravity modeling) including the  
739 respective boundary conditions and/or material properties. Detailed field as well as high-  
740 resolution analogue- and numerical- modeling studies will be key to addressing this question.

## 741 **5 Conclusions**

742 In this study, we have investigated how the variability in the size, orientation, depth and overall  
743 geometry of pre-existing weak zones influence the structural style and pattern of strain  
744 localization during rifting. We achieved this through a series of extensional analogue models  
745 consisting of weak zone made from silicone oil that is placed inside a layer of quartz sand,  
746 mimicking a brittle crust with inherited weak zone. We deployed digital image correlation  
747 technique to monitor the progressive surface deformation, allowing the cumulative horizontal  
748 displacement to be constrained at a high resolution. Our results have implication for improving

749 the understanding of the role of inherited structures, specifically crustal shear zones on rifts and  
750 rift-related faulting. Our key findings may be summarized as follows:

- 751 1. The presence of pre-existing weak zones in the brittle crust reduces the integrated  
752 strength of the crust that may facilitate strain localization in the vicinity of the weakened  
753 crust, resulting in the formation of rift graben. The graben is bounded by new faults  
754 whose geometries are influenced by the orientation of the pre-existing weak zones when  
755 the weak zone is oriented at  $\geq 60^\circ$  to the extension direction. The scale of the weak zone  
756 becomes an important factor when it is oriented at a much lower angle ( $\leq 45^\circ$ ) to the  
757 extension direction, in which case only large-scale weak zones may effectively weaken  
758 the crust and localize strain. Additionally, shallow weak zones are more likely to  
759 influence the pattern of deformation in the cover during subsequent rifting compared to  
760 deep weak zones. These observations underscore how different properties of a pre-  
761 existing weak zone may interplay to control its influence during rifting.
- 762 2. The timing of faulting and the amount of strain accommodated by graben-bounding  
763 faults are influenced by the orientation, size, or the depth of pre-existing weak zone.  
764 Graben-bounding faults nucleate earlier and accommodate more normal strain when the  
765 weak zone is: (i) oriented orthogonal to the extension direction compared to oblique  
766 orientation, (ii) large-scale compared to small-scale, and (iii) shallow compared to  
767 deeply buried.
- 768 3. Strain is mainly accommodated by pure dip-slip on normal faults, when the weak zone  
769 is orthogonal to the extension direction (i.e., orthogonal rift). Whereas, when the weak  
770 zone is oblique to the extension direction (i.e., oblique rift), strain is partitioned  
771 (increasing partitioning with increasing obliquity) into: (i) graben-bounding faults  
772 characterized by oblique-slip motion (i.e., major dip-slip, with minor component of  
773 strike-slip), and (ii) intra-graben domain dominated by strike-slip structures.

774 4. Under oblique extension, intra-graben faults that are orthogonal to the extension  
775 direction, initiates as strike-slip, antithetic Riedel shears.

## 776 **Acknowledgments, Samples, and Data**

777 This research forms part of the Syn-Rift Systems Project funded by the Research Council of  
778 Norway (project number 255229), Aker  
779 BP, ConocoPhillips, DNO, Equinor, Neptune and Tullow Oil to the University of Bergen and  
780 academic partners the universities of Leeds, East Anglia, Lorraine and the National and  
781 Kapodistrian University of Athens. We thank DEEP Research School, Norway, and Erasmus+  
782 for supporting the research stay of Edoseghe at GFZ Potsdam, Germany. Michael Rudolf has  
783 been supported by Deutsche Forschungsgemeinschaft (DFG) through grant CRC 1114 "Scaling  
784 Cascades in Complex Systems", Project Number 235221301, Project B01. We also thank the  
785 Norwegian Academy of Science and Letters for supporting Gawthorpe's VISTA Professorship  
786 which also provided a visiting researcher scholarship to Edoseghe. We thank Iverna Creton for  
787 laboratory assistance and stimulating discussions. Frank Neumann and Thomas Ziegenhagen  
788 are thanked for engineering and technical assistance. We also thank Sebastian Wolf for  
789 constructive discussions and suggestions during the preparation of the manuscript. We thank  
790 the reviewers Frank Zwaan, two anonymous reviewers, an anonymous associate editor, and  
791 Editor Laurent Jolivet for their constructive feedback and suggestions that significantly  
792 improved the manuscript. We thank GFZ data services for publishing the data underlying this  
793 Study.

794 All data underlying this study will be available in a GFZ Data Services open access  
795 publication (Osagiede et al., 2020b). \_\_\_\_\_

796 \_\_\_\_\_  
797 \_\_\_\_\_

- 799 Aanyu, K., & Koehn, D. (2011). Influence of pre-existing fabrics on fault kinematics and rift geometry of  
800 interacting segments: analogue models based on the Albertine Rift (Uganda), Western Branch-East  
801 African Rift System. *Journal of African Earth Sciences*, 59(2-3), 168-184.
- 802 Ackermann, R. V., & Schlische, R. W. (1997). Anticlustering of small normal faults around larger faults.  
803 *Geology*, 25(12), 1127-1130.
- 804 Adam, J., Urai, J., Wieneke, B., Oncken, O., Pfeiffer, K., Kukowski, N., Lohrmann, J., Hoth, S., Van Der Zee,  
805 W., & Schmatz, J. (2005). Shear localisation and strain distribution during tectonic faulting—New  
806 insights from granular-flow experiments and high-resolution optical image correlation techniques.  
807 *Journal of Structural Geology*, 27(2), 283-301.
- 808 Agostini, A., Bonini, M., Corti, G., Sani, F., & Mazzarini, F. (2011). Fault architecture in the Main Ethiopian  
809 Rift and comparison with experimental models: implications for rift evolution and Nubia–Somalia  
810 kinematics. *Earth and Planetary Science Letters*, 301(3-4), 479-492.
- 811 Agostini, A., Corti, G., Zeoli, A., & Mulugeta, G. (2009). Evolution, pattern, and partitioning of deformation  
812 during oblique continental rifting: Inferences from lithospheric-scale centrifuge models. *Geochemistry,  
813 Geophysics, Geosystems*, 10(11).
- 814 Allemand, P., & Brun, J.-P. (1991). Width of continental rifts and rheological layering of the lithosphere.  
815 *Tectonophysics*, 188(1-2), 63-69.
- 816 Allken, V., Huisman, R. S., & Thieulot, C. (2012). Factors controlling the mode of rift interaction in brittle-  
817 ductile coupled systems: A 3D numerical study. *Geochemistry, Geophysics, Geosystems*, 13(5).
- 818 Autin, J., Bellahsen, N., Husson, L., Beslier, M. o., Leroy, S., & d'Acremont, E. (2010). Analog models of  
819 oblique rifting in a cold lithosphere. *Tectonics*, 29(6).
- 820 Autin, J., Bellahsen, N., Leroy, S., Husson, L., Beslier, M.-O., & d'Acremont, E. (2013). The role of structural  
821 inheritance in oblique rifting: Insights from analogue models and application to the Gulf of Aden.  
822 *Tectonophysics*, 607, 51-64.
- 823 Bahroudi, A., Koyi, H. A., & Talbot, C. J. (2003). Effect of ductile and frictional décollements on style of  
824 extension. *Journal of Structural Geology*, 25(9), 1401-1423.
- 825 Bartholomew, I., Peters, J., & Powell, C. (1993). *Regional structural evolution of the North Sea: oblique slip and  
826 the reactivation of basement lineaments*. Paper presented at the Geological Society, London, Petroleum  
827 Geology Conference series.
- 828 Basile, C., & Brun, J. P. (1999). Transtensional faulting patterns ranging from pull-apart basins to transform  
829 continental margins: an experimental investigation. *Journal of Structural Geology*, 21(1), 23-37.
- 830 Bellahsen, N., Daniel, J.-M., Bollinger, L., & Burov, E. (2003). Influence of viscous layers on the growth of  
831 normal faults: insights from experimental and numerical models. *Journal of Structural Geology*, 25(9),  
832 1471-1485.
- 833 Bellahsen, N., & Daniel, J. M. (2005). Fault reactivation control on normal fault growth: an experimental study.  
834 *Journal of Structural Geology*, 27(4), 769-780.
- 835 Boccaletti, M., Bonini, M., Mazzuoli, R., Abebe, B., Piccardi, L., & Tortorici, L. (1998). Quaternary oblique  
836 extensional tectonics in the Ethiopian Rift (Horn of Africa). *Tectonophysics*, 287(1-4), 97-116.
- 837 Bonini, L., Basili, R., Toscani, G., Burrato, P., Seno, S., & Valensise, G. (2015). The role of pre-existing  
838 discontinuities in the development of extensional faults: an analog modeling perspective. *Journal of  
839 Structural Geology*, 74, 145-158.
- 840 Bonini, M., Cerca, M., Moratti, G., López-Martínez, M., Corti, G., & Gracia-Marroquín, D. (2019). Strain  
841 partitioning in highly oblique rift settings: Inferences from the southwestern margin of the Gulf of  
842 California (Baja California Sur, México). *Tectonics*, 38(12), 4426-4453.
- 843 Bonini, M., Souriot, T., Boccaletti, M., & Brun, J. P. (1997). Successive orthogonal and oblique extension  
844 episodes in a rift zone: Laboratory experiments with application to the Ethiopian Rift. *Tectonics*, 16(2),  
845 347-362.
- 846 Brun, J. P. (1999). Narrow rifts versus wide rifts: inferences for the mechanics of rifting from laboratory  
847 experiments. *Philosophical Transactions of the Royal Society of London. Series A: Mathematical,  
848 Physical and Engineering Sciences*, 357(1753), 695-712.
- 849 Brune, S. (2014). Evolution of stress and fault patterns in oblique rift systems: 3-D numerical lithospheric-scale  
850 experiments from rift to breakup. *Geochemistry, Geophysics, Geosystems*, 15(8), 3392-3415.
- 851 Brune, S., & Autin, J. (2013). The rift to break-up evolution of the Gulf of Aden: Insights from 3D numerical  
852 lithospheric-scale modelling. *Tectonophysics*, 607, 65-79.
- 853 Brune, S., Corti, G., & Ranalli, G. (2017). Controls of inherited lithospheric heterogeneity on rift linkage:  
854 Numerical and analog models of interaction between the Kenyan and Ethiopian rifts across the Turkana  
855 depression. *Tectonics*, 36(9), 1767-1786.

- 856 Brune, S., Popov, A. A., & Sobolev, S. V. (2012). Modeling suggests that oblique extension facilitates rifting  
857 and continental break-up. *Journal of Geophysical Research: Solid Earth*, 117(B8).
- 858 Chattopadhyay, A., & Chakra, M. (2013). Influence of pre-existing pervasive fabrics on fault patterns during  
859 orthogonal and oblique rifting: an experimental approach. *Marine and Petroleum Geology*, 39(1), 74-  
860 91.
- 861 Chemenda, A., Déverchère, J., & Calais, E. (2002). Three-dimensional laboratory modelling of rifting:  
862 application to the Baikal Rift, Russia. *Tectonophysics*, 356(4), 253-273.
- 863 Claringbould, J. S., Bell, R. E., Jackson, C. A.-L., Gawthorpe, R. L., & Odinsen, T. (2017). Pre-existing normal  
864 faults have limited control on the rift geometry of the northern North Sea. *Earth and Planetary Science  
865 Letters*, 475, 190-206.
- 866 Clifton, A. E., Schlische, R. W., Withjack, M. O., & Ackermann, R. V. (2000). Influence of rift obliquity on  
867 fault-population systematics: results of experimental clay models. *Journal of Structural Geology*,  
868 22(10), 1491-1509.
- 869 Collanega, L., Siuda, K., Jackson, C. A. L., Bell, R. E., Coleman, A. J., Lenhart, A., Magee, C., & Breda, A.  
870 (2019). Normal fault growth influenced by basement fabrics: the importance of preferential nucleation  
871 from pre-existing structures. *Basin Research*, 31, 659-687. doi:10.1111/bre.12327
- 872 Corti, G. (2004). Centrifuge modelling of the influence of crustal fabrics on the development of transfer zones:  
873 insights into the mechanics of continental rifting architecture. *Tectonophysics*, 384(1-4), 191-208.
- 874 Corti, G. (2008). Control of rift obliquity on the evolution and segmentation of the main Ethiopian rift. *Nature  
875 Geoscience*, 1(4), 258-262.
- 876 Corti, G. (2009). Continental rift evolution: from rift initiation to incipient break-up in the Main Ethiopian Rift,  
877 East Africa. *Earth-Science Reviews*, 96(1-2), 1-53.
- 878 Corti, G. (2012). Evolution and characteristics of continental rifting: Analog modeling-inspired view and  
879 comparison with examples from the East African Rift System. *Tectonophysics*, 522, 1-33.
- 880 Corti, G., Bonini, M., Innocenti, F., Manetti, P., & Mulugeta, G. (2001). Centrifuge models simulating magma  
881 emplacement during oblique rifting. *Journal of Geodynamics*, 31(5), 557-576.
- 882 Corti, G., Philippon, M., Sani, F., Keir, D., & Kidane, T. (2013). Re-orientation of the extension direction and  
883 pure extensional faulting at oblique rift margins: Comparison between the Main Ethiopian Rift and  
884 laboratory experiments. *Terra Nova*, 25(5), 396-404.
- 885 Corti, G., Van Wijk, J., Bonini, M., Sokoutis, D., Cloetingh, S., Innocenti, F., & Manetti, P. (2003). Transition  
886 from continental break-up to punctiform seafloor spreading: How fast, symmetric and magmatic.  
887 *Geophysical Research Letters*, 30(12).
- 888 Corti, G., van Wijk, J., Cloetingh, S., & Morley, C. K. (2007). Tectonic inheritance and continental rift  
889 architecture: Numerical and analogue models of the East African Rift system. *Tectonics*, 26(6), 1-13.  
890 doi:10.1029/2006TC002086
- 891 Cowie, P. (1998). A healing–reloading feedback control on the growth rate of seismogenic faults. *Journal of  
892 Structural Geology*, 20(8), 1075-1087.
- 893 Daly, M., Chorowicz, J., & Fairhead, J. (1989). Rift basin evolution in Africa: the influence of reactivated steep  
894 basement shear zones. *Geological Society, London, Special Publications*, 44(1), 309-334.
- 895 Dauteuil, O., & Brun, J.-P. (1993). Oblique rifting in a slow-spreading ridge. *Nature*, 361(6408), 145-148.
- 896 Dauteuil, O., & Brun, J. P. (1996). Deformation partitioning in a slow spreading ridge undergoing oblique  
897 extension: Mohns Ridge, Norwegian Sea. *Tectonics*, 15(4), 870-884.
- 898 Dauteuil, O., Huchon, P., Quemeneur, F., & Souriot, T. (2001). Propagation of an oblique spreading centre: the  
899 western Gulf of Aden. *Tectonophysics*, 332(4), 423-442.
- 900 Dautriat, J., Bornert, M., Gland, N., Dimanov, A., & Raphanel, J. (2011). Localized deformation induced by  
901 heterogeneities in porous carbonate analysed by multi-scale digital image correlation. *Tectonophysics*,  
902 503(1-2), 100-116.
- 903 Dawson, S. M., Laó-Dávila, D. A., Atekwana, E. A., & Abdelsalam, M. G. (2018). The influence of the  
904 Precambrian Mughese Shear Zone structures on strain accommodation in the northern Malawi Rift.  
905 *Tectonophysics*, 722, 53-68.
- 906 de Castro, D., Bezerra, F., Fuck, R., & Vidotti, R. (2016). Geophysical evidence of pre-sag rifting and post-  
907 rifting fault reactivation in the Parnaíba basin, Brazil. *Solid Earth*, 7, 529-548. doi:10.5194/se-7-529-  
908 2016
- 909 Del Ventisette, C., Bonini, M., Agostini, A., Corti, G., Maestrelli, D., & Montanari, D. (2019). Using different  
910 grain-size granular mixtures (quartz and K-feldspar sand) in analogue extensional models. *Journal of  
911 Structural Geology*, 103888. doi:https://doi.org/10.1016/j.jsg.2019.103888
- 912 Deng, C., Gawthorpe, R. L., Finch, E., & Fossen, H. (2017). Influence of a pre-existing basement weakness on  
913 normal fault growth during oblique extension: Insights from discrete element modeling. *Journal of  
914 Structural Geology*, 105, 44-61.

915 Duclaux, G., Huisman, R. S., & May, D. A. (2020). Rotation, narrowing, and preferential reactivation of brittle  
916 structures during oblique rifting. *Earth and Planetary Science Letters*, 531, 115952.

917 Dunbar, J. A., & Sawyer, D. S. (1988). Continental rifting at pre-existing lithospheric weaknesses. *Nature*,  
918 333(6172), 450-452.

919 Dyksterhuis, S., Rey, P., Müller, R., & Moresi, L. (2007). Effects of initial weakness on rift architecture.  
920 *Geological Society, London, Special Publications*, 282(1), 443-455.

921 Fazlikhani, H., & Back, S. (2015). The influence of pre-existing structure on the growth of syn-sedimentary  
922 normal faults in a deltaic setting, Niger Delta. *Journal of Structural Geology*, 73, 18-32.  
923 doi:<http://dx.doi.org/10.1016/j.jsg.2015.01.011>

924 Fazlikhani, H., Fossen, H., Gawthorpe, R. L., Faleide, J., & Bell, R. E. (2017). Basement structure and its  
925 influence on the structural configuration of the northern North Sea.

926 Ge, Z., Rosenau, M., Warsitzka, M., & Gawthorpe, R. L. (2019). Overprinting translational domains in passive  
927 margin salt basins: insights from analogue modelling. *Solid Earth*, 10(4), 1283-1300.

928 Ghosh, N., Hatui, K., & Chattopadhyay, A. (2020). Evolution of fault patterns within a zone of pre-existing  
929 pervasive anisotropy during two successive phases of extensions: an experimental study. *Geo-Marine  
930 Letters*, 40(1), 53-74.

931 Gibson, G. M., Totterdell, J., White, L. T., Mitchell, C., Stacey, A., Morse, M., & Whitaker, A. (2013). Pre-  
932 existing basement structure and its influence on continental rifting and fracture zone development along  
933 Australia's southern rifted margin. *Journal of the Geological Society*, 170(2), 365-377.

934 Gupta, A., & Scholz, C. H. (2000). A model of normal fault interaction based on observations and theory.  
935 *Journal of Structural Geology*, 22(7), 865-879.

936 Heilman, E., Kolawole, F., Atekwana, E. A., & Mayle, M. (2019). Controls of Basement Fabric on the Linkage  
937 of Rift Segments. *Tectonics*, 38(4), 1337-1366.

938 Henza, A. A., Withjack, M. O., & Schlische, R. W. (2010). Normal-fault development during two phases of non-  
939 coaxial extension: An experimental study. *Journal of Structural Geology*, 32(11), 1656-1667.

940 Hubbert, M. K. (1937). Theory of scale models as applied to the study of geologic structures. *Geological Society  
941 of America Bulletin*, 48(10), 1459-1520.

942 Keep, M., & McClay, K. (1997). Analogue modelling of multiphase rift systems. *Tectonophysics*, 273(3), 239-  
943 270.

944 Kirkpatrick, J., Bezerra, F., Shipton, Z., Do Nascimento, A., Pytharouli, S., Lunn, R., & Soden, A. (2013). Scale-  
945 dependent influence of pre-existing basement shear zones on rift faulting: a case study from NE Brazil.  
946 *Journal of the Geological Society*, 170(2), 237-247.

947 Klinkmüller, M., Schreurs, G., Rosenau, M., & Kemnitz, H. (2016). Properties of granular analogue model  
948 materials: A community wide survey. *Tectonophysics*, 684, 23-38.

949 Kolawole, F., Atekwana, E. A., Laó-Dávila, D. A., Abdelsalam, M. G., Chindandali, P. R., Salima, J., &  
950 Kalindekaffe, L. (2018). Active deformation of Malawi rift's north basin Hinge zone modulated by  
951 reactivation of preexisting Precambrian Shear zone fabric. *Tectonics*, 37(3), 683-704.

952 Le Calvez, J. H., & Vendeville, B. C. (2002). Physical modeling of normal faults and graben relays above salt: A  
953 qualitative and quantitative analysis. *Gulf Coast Association of Geological Societies Transactions*, 52,  
954 599 - 606.

955 Lohrmann, J., Kukowski, N., Adam, J., & Oncken, O. (2003). The impact of analogue material properties on the  
956 geometry, kinematics, and dynamics of convergent sand wedges. *Journal of Structural Geology*, 25(10),  
957 1691-1711.

958 Maerten, L., Gillespie, P., & Pollard, D. D. (2002). Effects of local stress perturbation on secondary fault  
959 development. *Journal of Structural Geology*, 24(1), 145-153.

960 Maestrelli, D., Montanari, D., Corti, G., Del Ventisette, C., Moratti, G., & Bonini, M. (2020). Exploring the  
961 Interactions Between Rift Propagation and Inherited Crustal Fabrics Through Experimental Modeling.  
962 *Tectonics*, 39(12), e2020TC006211.

963 Maniatis, G., & Hampel, A. (2008). Along-strike variations of the slip direction on normal faults: Insights from  
964 three-dimensional finite-element models. *Journal of Structural Geology*, 30(1), 21-28.

965 Maurin, J.-C., & Guiraud, R. (1993). Basement control in the development of the Early Cretaceous West and  
966 Central African rift system. *Tectonophysics*, 228(1-2), 81-95.

967 McClay, K., Dooley, T., Whitehouse, P., & Mills, M. (2002). 4-D evolution of rift systems: Insights from scaled  
968 physical models. *AAPG Bulletin*, 86(6), 935-959.

969 McClay, K., & White, M. (1995). Analogue modelling of orthogonal and oblique rifting. *Marine and Petroleum  
970 Geology*, 12(2), 137-151.

971 McConnell, R. B. (1967). The east African rift system. *Nature*, 215(5101), 578-581.

972 Michon, L., & Merle, O. (2000). Crustal structures of the Rhinegraben and the Massif Central grabens: An  
973 experimental approach. *Tectonics*, 19(5), 896-904.



974 Michon, L., & Sokoutis, D. (2005). Interaction between structural inheritance and extension direction during  
975 graben and depocentre formation: An experimental approach. *Tectonophysics*, 409(1-4), 125-146.

976 Molnar, N., Cruden, A., & Betts, P. (2020). The role of inherited crustal and lithospheric architecture during the  
977 evolution of the Red Sea: Insights from three dimensional analogue experiments. *Earth and Planetary  
978 Science Letters*, 544, 116377.

979 Molnar, N. E., Cruden, A. R., & Betts, P. G. (2019). Interactions between propagating rifts and linear  
980 weaknesses in the lower crust. *Geosphere*, 15(5), 1617-1640.

981 Morley, C. (1995). Developments in the structural geology of rifts over the last decade and their impact on  
982 hydrocarbon exploration. *Geological Society, London, Special Publications*, 80(1), 1-32.

983 Morley, C. (2010). Stress re-orientation along zones of weak fabrics in rifts: An explanation for pure extension  
984 in ‘oblique’ rift segments? *Earth and Planetary Science Letters*, 297(3-4), 667-673.

985 Morley, C., Haranya, C., Phoosongsee, W., Pongwapee, S., Kornsawan, A., & Wonganan, N. (2004). Activation  
986 of rift oblique and rift parallel pre-existing fabrics during extension and their effect on deformation  
987 style: examples from the rifts of Thailand. *Journal of Structural Geology*, 26(10), 1803-1829.

988 Muirhead, J., & Kattenhorn, S. (2018). Activation of preexisting transverse structures in an evolving magmatic  
989 rift in East Africa. *Journal of Structural Geology*, 106, 1-18.

990 Mulugeta, G. (1988). Squeeze box in a centrifuge. *Tectonophysics*, 148(3-4), 323-335.

991 Osagiede, E. E., Rosenau, M., Rudolf, M., Rotevatn, A., Gawthorpe, R., & Jackson, C. A.-L. (2020b). Digital  
992 image correlation data from analogue modelling experiments addressing extension of weakened crust.  
993 *GFZ Data Services*. doi:<http://doi.org/10.5880/GFZ.4.1.2020.005>

994 Osagiede, E. E., Rotevatn, A., Gawthorpe, R., Kristensen, T. B., Jackson, C. A., & Marsh, N. (2020a). Pre-  
995 existing intra-basement shear zones influence growth and geometry of non-colinear normal faults,  
996 western Utsira High–Heimdal Terrace, North Sea. *Journal of Structural Geology*, 130, 103908.

997 Panien, M., Schreurs, G., & Pfiffner, A. (2006). Mechanical behaviour of granular materials used in analogue  
998 modelling: insights from grain characterisation, ring-shear tests and analogue experiments. *Journal of  
999 Structural Geology*, 28(9), 1710-1724.

1000 Peacock, D., Nixon, C., Rotevatn, A., Sanderson, D., & Zuluaga, L. (2016). Glossary of fault and other fracture  
1001 networks. *Journal of Structural Geology*, 92, 12-29.

1002 Philippon, M., & Corti, G. (2016). Obliquity along plate boundaries. *Tectonophysics*, 693, 171-182.

1003 Philippon, M., Willingshofer, E., Sokoutis, D., Corti, G., Sani, F., Bonini, M., & Cloetingh, S. (2015). Slip re-  
1004 orientation in oblique rifts. *Geology*, 43(2), 147-150.

1005 Phillips, T. B., Fazlikhani, H., Gawthorpe, R. L., Fossen, H., Jackson, C. A. L., Bell, R. E., Faleide, J. I., &  
1006 Rotevatn, A. (2019). The Influence of Structural Inheritance and Multiphase Extension on Rift  
1007 Development, the Northern North Sea. *Tectonics*.

1008 Phillips, T. B., Jackson, C. A. L., Bell, R. E., Duffy, O. B., & Fossen, H. (2016). Reactivation of intrabasement  
1009 structures during rifting: A case study from offshore southern Norway. *Journal of Structural Geology*,  
1010 91, 54-73. doi:<http://dx.doi.org/10.1016/j.jsg.2016.08.008>

1011 Ramberg, H. (1981). *Gravity, deformation and the earth's crust: in theory, experiments and geological  
1012 application*: Academic press.

1013 Ranalli, G., & Yin, Z.-M. (1990). Critical stress difference and orientation of faults in rocks with strength  
1014 anisotropies: the two-dimensional case. *Journal of Structural Geology*, 12(8), 1067-1071.

1015 Reeve, M. T., Bell, R. E., Duffy, O. B., Jackson, C. A. L., & Sansom, E. (2015). The growth of non-colinear  
1016 normal fault systems; What can we learn from 3D seismic reflection data? *Journal of Structural  
1017 Geology*, 70, 141-155. doi:<http://dx.doi.org/10.1016/j.jsg.2014.11.007>

1018 Reeve, M. T., Bell, R. E., & Jackson, C. A.-L. (2013). Origin and significance of intra-basement seismic  
1019 reflections offshore western Norway. *Journal of the Geological Society*, 171(1), 1-4.

1020 Ring, U. (1994). The influence of preexisting structure on the evolution of the Cenozoic Malawi rift (East  
1021 African rift system). *Tectonics*, 13(2), 313-326.

1022 Ritter, M. C., Leever, K., Rosenau, M., & Oncken, O. (2016). Scaling the sandbox—Mechanical (dis)  
1023 similarities of granular materials and brittle rock. *Journal of Geophysical Research: Solid Earth*,  
1024 121(9), 6863-6879.

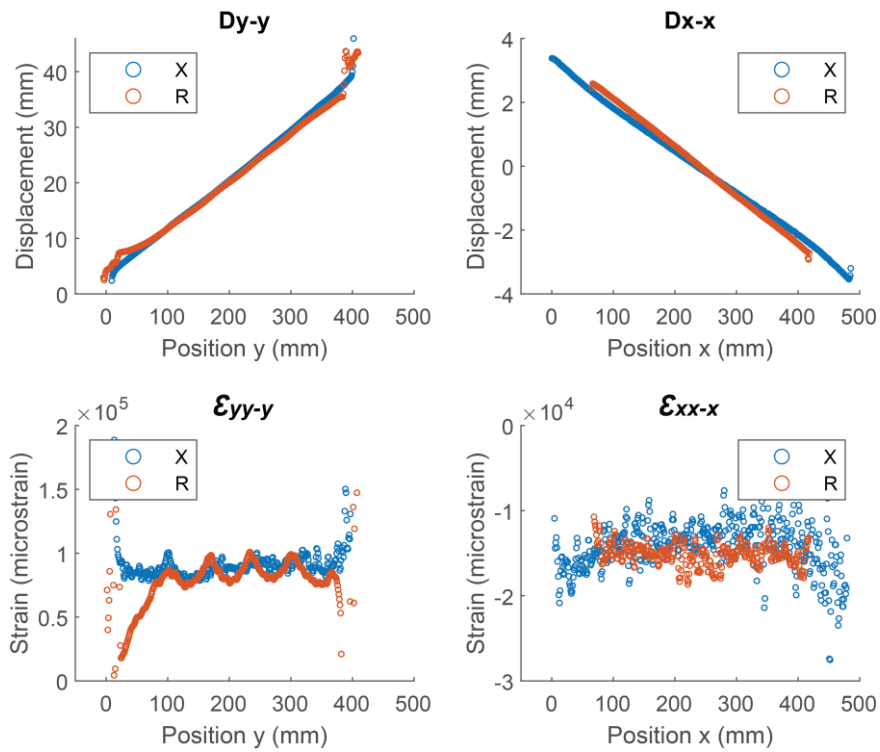
1025 Rosenau, M., Pohlenz, A., Kemnitz, H., & Warsitzka, M. (2018). Ring-shear test data of quartz sand G12 used  
1026 for analogue experiments in the Helmholtz Laboratory for Tectonic Modelling (HelTec) at the GFZ  
1027 German Research Centre for Geosciences in Potsdam. *GFZ Data Services*.  
1028 doi:<http://doi.org/10.5880/GFZ.4.1.2019.003>

1029 Rotevatn, A., Kristensen, T., Ksienzyk, A., Wemmer, K., Henstra, G., Midtkandal, I., Grundvåg, S. A., &  
1030 Andresen, A. (2018). Structural inheritance and rapid rift-length establishment in a multiphase rift: the  
1031 East Greenland rift system and its Caledonian orogenic ancestry. *Tectonics*, 37, 1858-1875.

- 1032 Rudolf, M., Boutelier, D., Rosenau, M., Schreurs, G., & Oncken, O. (2016). Rheological benchmark of silicone  
1033 oils used for analog modeling of short-and long-term lithospheric deformation. *Tectonophysics*, 684,  
1034 12-22.
- 1035 Salomon, E., Koehn, D., & Passchier, C. (2015). Brittle reactivation of ductile shear zones in NW Namibia in  
1036 relation to South Atlantic rifting. *Tectonics*, 34(1), 70-85.
- 1037 Sani, F., Bonini, M., Corti, G., & Moratti, G. (2019). Extension direction re-orientation in the oceanic rift of  
1038 Iceland, and comparison with continental rifts. *Tectonophysics*, 756, 25-42.
- 1039 Saria, E., Calais, E., Stamps, D., Delvaux, D., & Hartnady, C. (2014). Present-day kinematics of the East African  
1040 Rift. *Journal of Geophysical Research: Solid Earth*, 119(4), 3584-3600.
- 1041 Schellart, W. (2000). Shear test results for cohesion and friction coefficients for different granular materials:  
1042 scaling implications for their usage in analogue modelling. *Tectonophysics*, 324(1-2), 1-16.
- 1043 Schellart, W. P., & Strak, V. (2016). A review of analogue modelling of geodynamic processes: Approaches,  
1044 scaling, materials and quantification, with an application to subduction experiments. *Journal of*  
1045 *Geodynamics*, 100, 7-32.
- 1046 Schlagenhauf, A., Manighetti, I., Malavieille, J., & Dominguez, S. (2008). Incremental growth of normal faults:  
1047 Insights from a laser-equipped analog experiment. *Earth and Planetary Science Letters*, 273(3-4), 299-  
1048 311.
- 1049 Scholz, C. H., & Contreras, J. C. (1998). Mechanics of continental rift architecture. *Geology*, 26(11), 967-970.
- 1050 Schreurs, G., Buitter, S. J., Boutelier, D., Corti, G., Costa, E., Cruden, A. R., Daniel, J., Hoth, S., Koyi, H. A., &  
1051 Kukowski, N. (2006). Analogue benchmarks of shortening and extension experiments. *Special*  
1052 *Publication-Geological Society Of London*, 253, 1.
- 1053 Schreurs, G., Buitter, S. J., Boutelier, J., Burberry, C., Callot, J.-P., Cavozi, C., Cerca, M., Chen, J.-H.,  
1054 Cristallini, E., & Cruden, A. R. (2016). Benchmarking analogue models of brittle thrust wedges.  
1055 *Journal of Structural Geology*, 92, 116-139.
- 1056 Sokoutis, D., Corti, G., Bonini, M., Brun, J. P., Cloetingh, S., Mauduit, T., & Manetti, P. (2007). Modelling the  
1057 extension of heterogeneous hot lithosphere. *Tectonophysics*, 444(1-4), 63-79.
- 1058 Soliva, R., Benedicto, A., & Maerten, L. (2006). Spacing and linkage of confined normal faults: importance of  
1059 mechanical thickness. *Journal of Geophysical Research: Solid Earth*, 111(B1).
- 1060 Sylvester, A. G. (1988). Strike-slip faults. *Geological Society of America Bulletin*, 100(11), 1666-1703.
- 1061 Theunissen, K., Klerkx, J., Melnikov, A., & Mruma, A. (1996). Mechanisms of inheritance of rift faulting in the  
1062 western branch of the East African Rift, Tanzania. *Tectonics*, 15(4), 776-790.
- 1063 Tong, H., Koyi, H., Huang, S., & Zhao, H. (2014). The effect of multiple pre-existing weaknesses on formation  
1064 and evolution of faults in extended sandbox models. *Tectonophysics*, 626, 197-212.
- 1065 Tron, V., & Brun, J.-P. (1991). Experiments on oblique rifting in brittle-ductile systems. *Tectonophysics*, 188(1-  
1066 2), 71-84.
- 1067 Van Wijk, J. (2005). Role of weak zone orientation in continental lithosphere extension. *Geophysical Research*  
1068 *Letters*, 32(2).
- 1069 Vauchez, A., Tommasi, A., & Barruol, G. (1998). Rheological heterogeneity, mechanical anisotropy and  
1070 deformation of the continental lithosphere. *Tectonophysics*, 296(1-2), 61-86.
- 1071 Versfelt, J., & Rosendahl, B. R. (1989). Relationships between pre-rift structure and rift architecture in Lakes  
1072 Tanganyika and Malawi, East Africa. *Nature*, 337(6205), 354-357.
- 1073 White, D. J., Take, W., & Bolton, M. (2001). Measuring soil deformation in geotechnical models using digital  
1074 images and PIV analysis. In *10th International Conference on Computer Methods and Advances in*  
1075 *Geomechanics, Tuscon, Arizona*(1), 997-1002.
- 1076 Withjack, M. O., & Jamison, W. R. (1986). Deformation produced by oblique rifting. *Tectonophysics*, 126(2-4),  
1077 99-124.
- 1078 Wrona, T., Fossen, H., Lecomte, I., Eide, C., & Gawthorpe, R. (2020). Seismic expression of shear zones:  
1079 Insights from 2-D point-spread-function-based convolution modelling. *Journal of Structural Geology*,  
1080 104121.
- 1081 Zwaan, F., Chenin, P., Erratt, D., Manatschal, G., & Schreurs, G. (in review). Complex rift patterns, a result of  
1082 interacting crustal and mantle weaknesses, or multiphase rifting? Insights from analogue models. *Solid*  
1083 *Earth Discussion (preprint)*, 1-38. doi:https://doi.org/10.5194/se-2020-214
- 1084 Zwaan, F., & Schreurs, G. (2017). How oblique extension and structural inheritance influence rift segment  
1085 interaction: Insights from 4D analog models. *Interpretation*, 5(1), SD119-SD138.
- 1086 Zwaan, F., Schreurs, G., & Buitter, S. (2019). A systematic comparison of experimental set-ups for modelling  
1087 extensional tectonics. *Solid Earth (SE)*, 10(4), 1063-1097.
- 1088 Zwaan, F., Schreurs, G., Naliboff, J., & Buitter, S. J. (2016). Insights into the effects of oblique extension on  
1089 continental rift interaction from 3D analogue and numerical models. *Tectonophysics*, 693, 239-260.
- 1090 Zwaan, F., Schreurs, G., & Rosenau, M. (2020). Rift propagation in rotational versus orthogonal extension:  
1091 Insights from 4D analogue models. *Journal of Structural Geology*, 135, 103946.

1092 **Appendix**

1093 **Appendix 1**



1094

1095 *Benchmarks verifying the basal boundary condition of distributed, non-plane strain pure shear:*  
1096 *The upper row shows final displacements after 50 mm of externally applied wall motion both*  
1097 *parallel (y, left) and normal (x, right) to the extension direction for the benchmark model X*  
1098 *(basal foam only) and reference model R (sand layer 40 mm thick). Displacement profiles are*  
1099 *linear and parallel suggesting first-order quantitative transfer of homogenous deformation*  
1100 *from the basal foam to the sand layer. Middle row shows the corresponding longitudinal strains*  
1101 *Eyy-y and Exx-y. Note that strain localization is unavoidable at the boundaries but the central*  
1102 *area of interest is homogeneously extended longitudinally by c. 8-10 % and shortened*  
1103 *transversally by c. 1.5 % resulting in a “Poisson rate” of c. 16%.*

1104 **Appendix 2**

1105 Calculation of strain from vector field and strain rate:

1106 The strain fields for normal strain  $\varepsilon_n$  and shear strain  $\varepsilon_s$  are calculated by LaVision DaVis as  
1107 the gradient in the vector field  $V_i$  with respect to the direction  $j$ , according to the strain tensor  
1108 (DaVis 10.1 Manual, 2019):

1109

1110  $\varepsilon_{ij} = \partial V_i / \partial j$  with  $i \in \{x, y\}$  and  $j \in \{x, y\}$

1111  
 1112  
 1113  
 1114  
 1115  
 1116  
 1117  
 1118  
 1119

The normal strain is the gradient in  $V_y$  along the y axis  $\epsilon_n = \epsilon_{yy}$  and therefore representative of compression or extension along the main deformation axis. The shear strain is the change in  $V_y$  along the x axis  $\epsilon_s = \epsilon_{xy}$  and represents horizontal shear. Because the vector field is on a discrete grid the strain tensor at a point  $(n, m)$  (where  $n$  is the matrix index in x and  $m$  in y direction) is approximated by taking the average between the neighbouring vectors  $V_y(n, m + 1)$  and  $V_y(n, m - 1)$  in the respective direction and multiplying it with the vector spacing  $d$ :

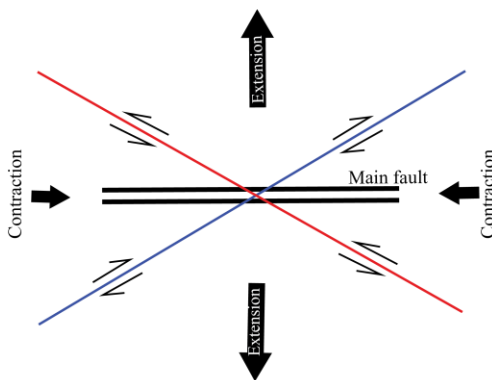
1120 
$$\epsilon_{xy}(n, m) = \frac{V_x(n, m + 1) - V_x(n, m - 1)}{2} \cdot d$$

1121

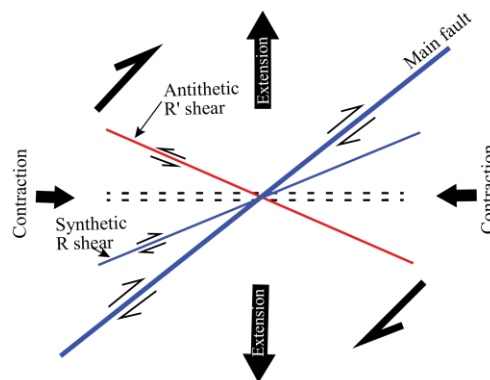
1122 At the edges of the vector field where one of the neighbouring points does not exist, the  
 1123 missing neighbour is replaced by the value at  $(n, m)$ . If neither exist, the strain is set to zero.  
 1124 To convert strain  $\epsilon$  into strain rates  $\dot{\epsilon}$  the values are multiplied by the time between images  
 1125  $\Delta t$ :  
 1126  $\dot{\epsilon} = \epsilon \cdot \Delta t$

1127 **Appendix 3**

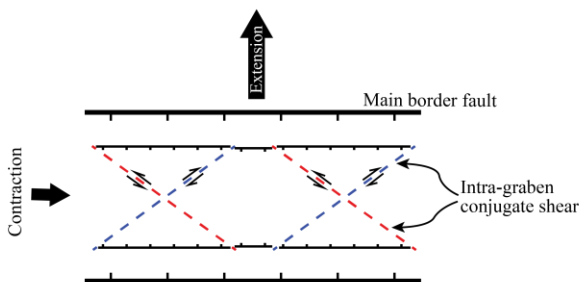
a) Pure shear



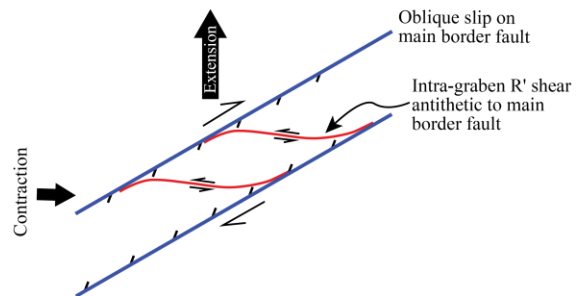
b) Simple shear



c) Orthogonal extension model (this study)



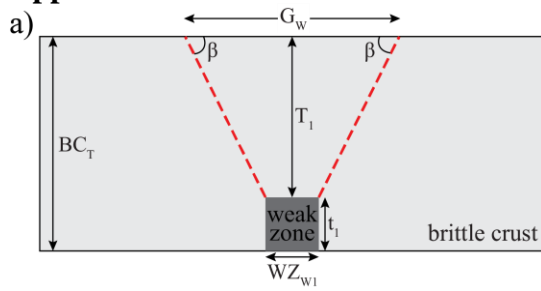
d) Oblique extension model (this study)



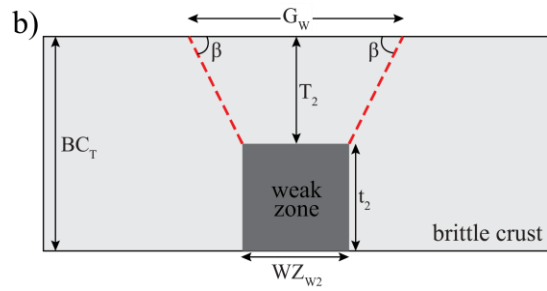
1128

1129 *Geometrical relationship of structures associated with pure shear and simple shear kinematics,*  
 1130 *and how they correlate with the major structures observed in our orthogonal and oblique*  
 1131 *models based on longitudinal and shear strain analysis (modified from Sylvester, 1988).*

1132 **Appendix 4**



$$\mathbf{G_w = WZ_{w1} + 2(T_1 \cot\beta)}$$



$$\mathbf{G_w = WZ_{w2} + 2(T_2 \cot\beta)}$$

1133

1134 *Geometrical relationship between graben width ( $G_w$ ), the weak zone width ( $WZ_w$ ), the*  
 1135 *thickness of the brittle layer above the weak zone ( $T$ ), and the dip of the graben-bounding*  
 1136 *faults ( $\beta$ ). The graben width is theoretically equal in (a) the small weak zone model and (b)*  
 1137 *the large weak zone model since the dip of the graben-bounding faults is the same. Modified*  
 1138 *from Corti (2004).*

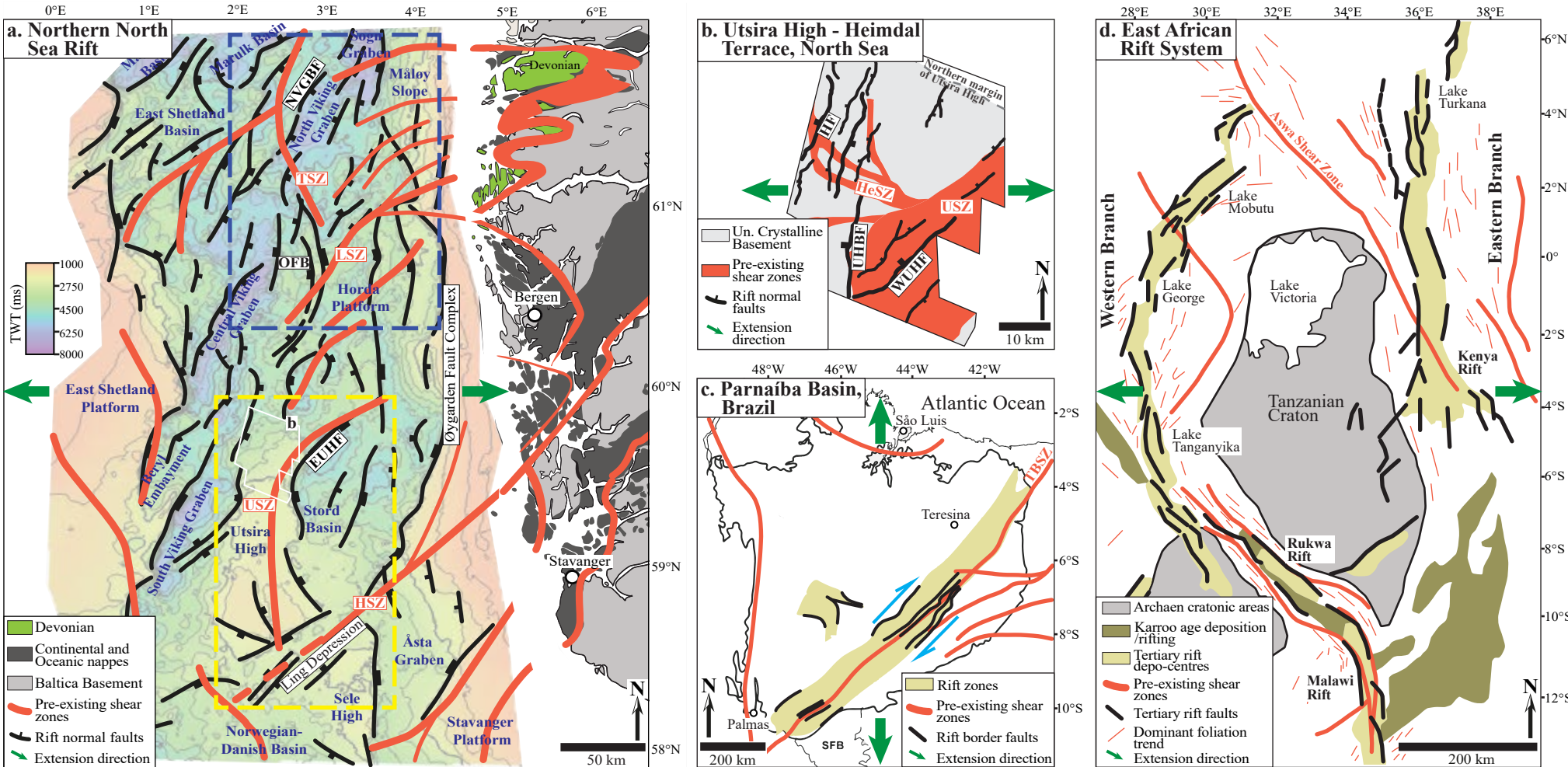


**Figure 1:** Simplified maps of natural rift systems showing the plan-view relationship between pre-existing shear zones and younger rift-related normal faults/graben structure across a range of scales. (a) Rift-scale: the northern North Sea Rift superimposed on a two-way-time (TWT) structure map at the base rift phase 1 structural level, showing; (i) area marked by the yellow stippled box, where younger rift-related faults and intra-rift graben mimic the plan-view geometry of the underlying pre-existing shear zones (e.g., the Eastern Utsira High Fault, EUHF and the Utsira Shear Zone, USZ; the Ling Depression and the Hardangerfjord Shear Zone, HSZ), and (ii) area marked by the blue stippled box, where younger rift-related faults are oblique to the underlying pre-existing shear zones (e.g., the Oseberg Fault Block, OFB and the Lomre Shear Zone, LSZ; the North Viking Graben Border Fault, NVGBF and the Tampen Shear Zone, TSZ) (modified from Phillips et al., 2019). (b) Fault array-scale: the Utsira High – Heimdal Terrace (see location in Fig. a) showing strong geometric correlation between the Western Utsira High Fault (WUHF) and the pre-existing Utsira Shear Zone, and obliqueness of the Utsira High Border Fault (UHBF) and Heimdal Fault (HF) with the pre-existing Heimdal Shear Zone (HeSZ) (modified from Osagiede et al., 2020a). (c) Basin-scale: the Parnaíba Basin, Brazil showing the correlation of the Parnaíba rift zone with the Transbrasiliiano Shear Zone (TBSZ) (modified from de Castro et al., 2016). (d) Rift-scale: the East African Rift System showing the correlation between the Rukwa – Malawi rift segments and the inter-cratonic mobile belt (modified from Morley, 1995).



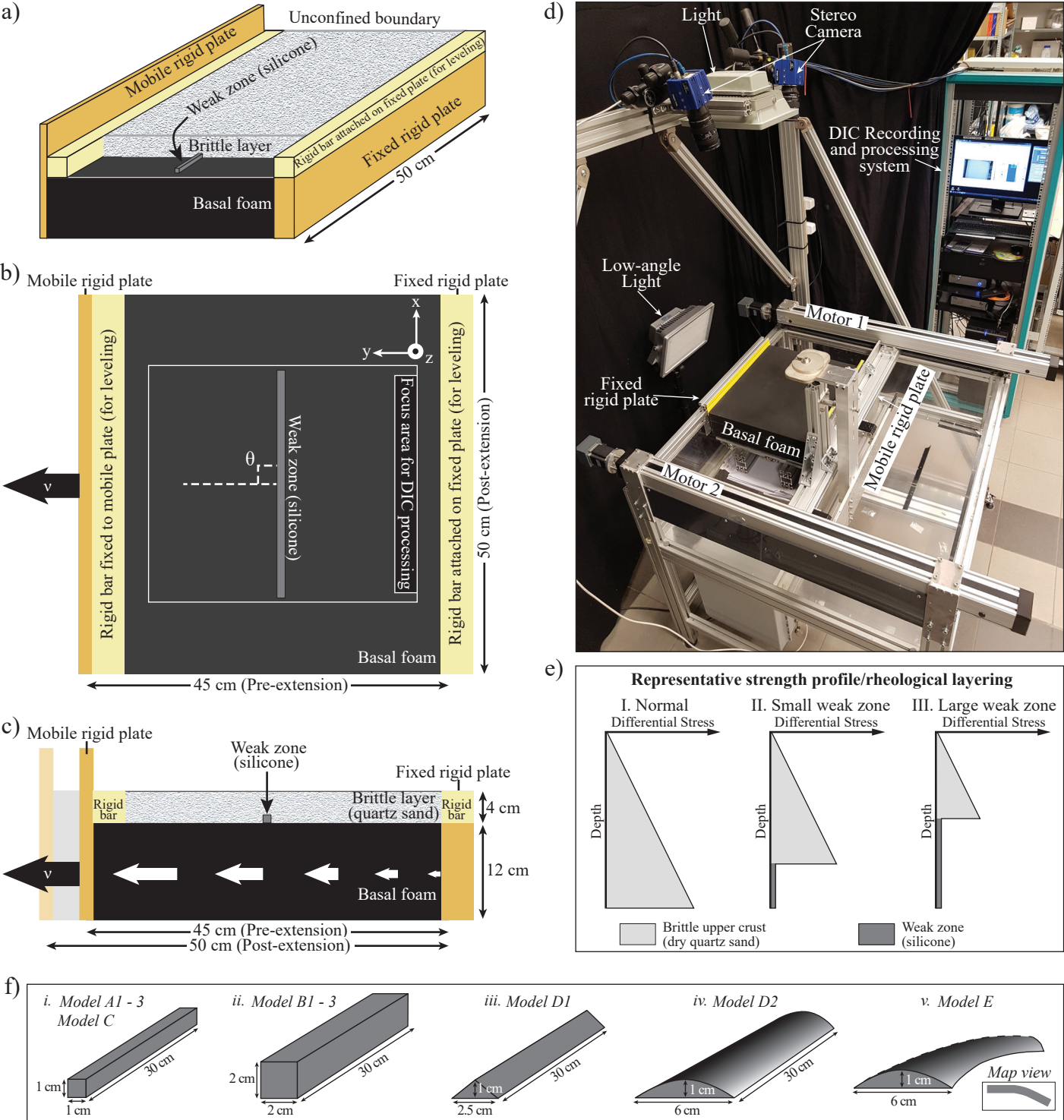


**Figure 2:** Model setup and apparatus. (a) 3D oblique view indicating the main components of our models. (b) Representative plan-view sketch of our weak zone geometry oriented at  $\theta = 90^\circ$  to the extension direction represented by the black arrow, and the focus area used for the time-series DIC processing. (c) Representative cross-sectional view, indicating our model layering and distributed deformation at the base of the models. (d) Experimental deformation rig-, recording-, and processing- setups. (e) Hypothetical rheological layering and associated strength profile for the normal (pristine)- and weakened- crust respectively, in our experimental series A (not drawn to scale). (f) The 3D geometry and dimensions of the weak zone used in the different models to simulate a range of natural weak zone geometries (note the map view insert of the weak zone in Model E).

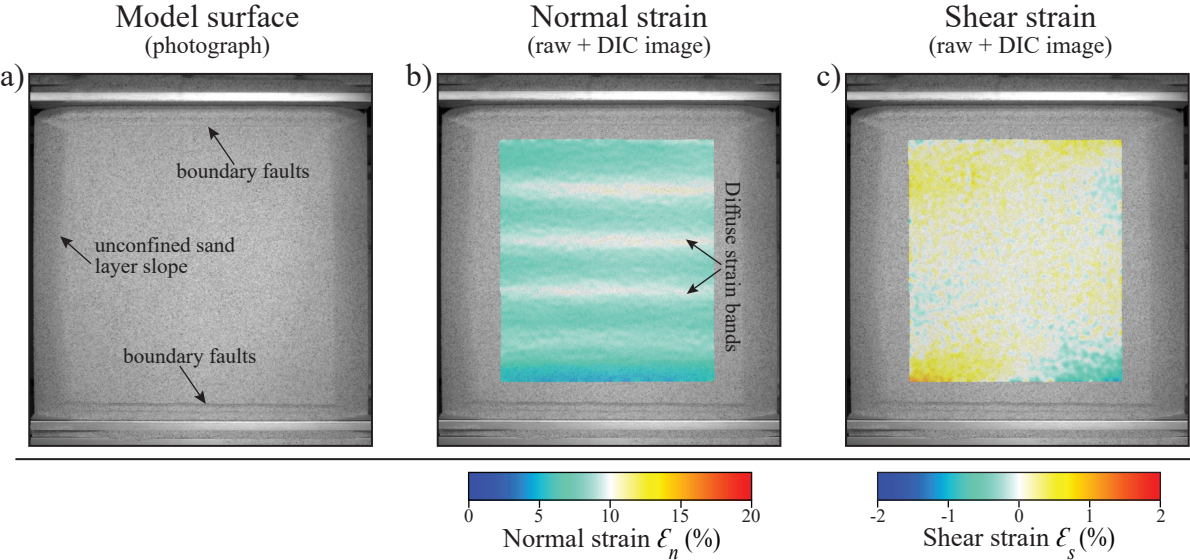


**Figure 3:** Reference model R consisting of a 4 cm brittle-layer above a basal foam. (a) post-extension image of the model surface characterized by boundary faults that mark ‘edge effect’. (b) DIC-derived normal strain component of the model centre (focus area) superimposed on the raw image. There is no strain localization except for the formation of ‘diffuse strain bands’ (see text for detail). (c) DIC-derived shear strain component of the model centre (focus area) superimposed on the raw image. Shear strain values are c. zero and chaotic.



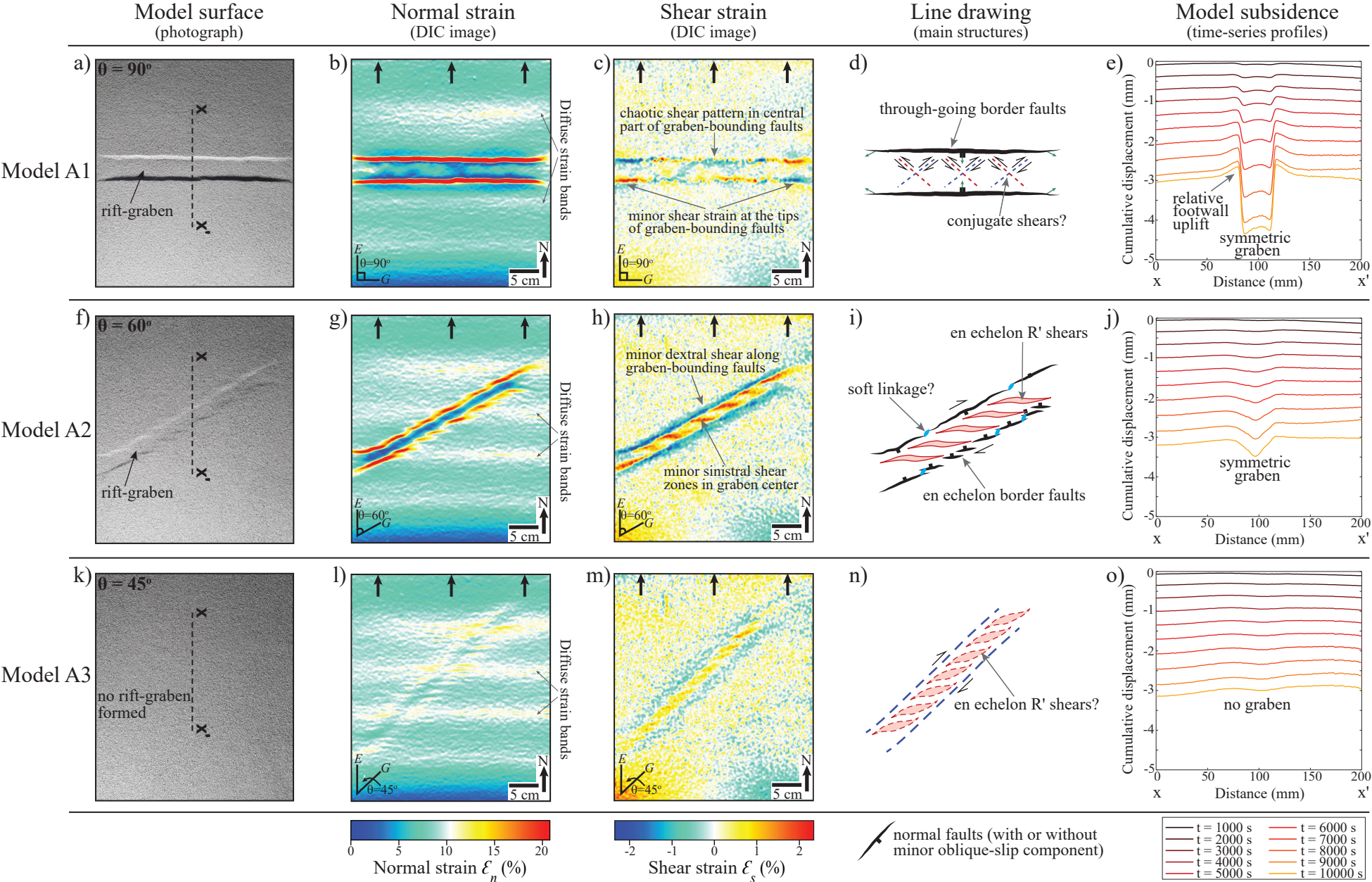


**Figure 4:** Final stage surface deformation of Experimental Series A (small weak zone); Model A1 ( $\theta = 90^\circ$ ), Model A2 ( $\theta = 60^\circ$ ), Model A3 ( $\theta = 45^\circ$ ). Panel consist of photograph of the central portion of model surface, corresponding DIC-derived normal and shear strain components, line drawing of the main normal and shear structures, and time-series model subsidence profiles. Locations of the subsidence profiles are indicated in the photographs (X - X'). The main structures are annotated and lateral exaggeration on the line drawings is 2x. E = extension direction, G = graben axis, t = time in seconds. Note that an apparent 'northern' direction is imposed for the purpose of description.



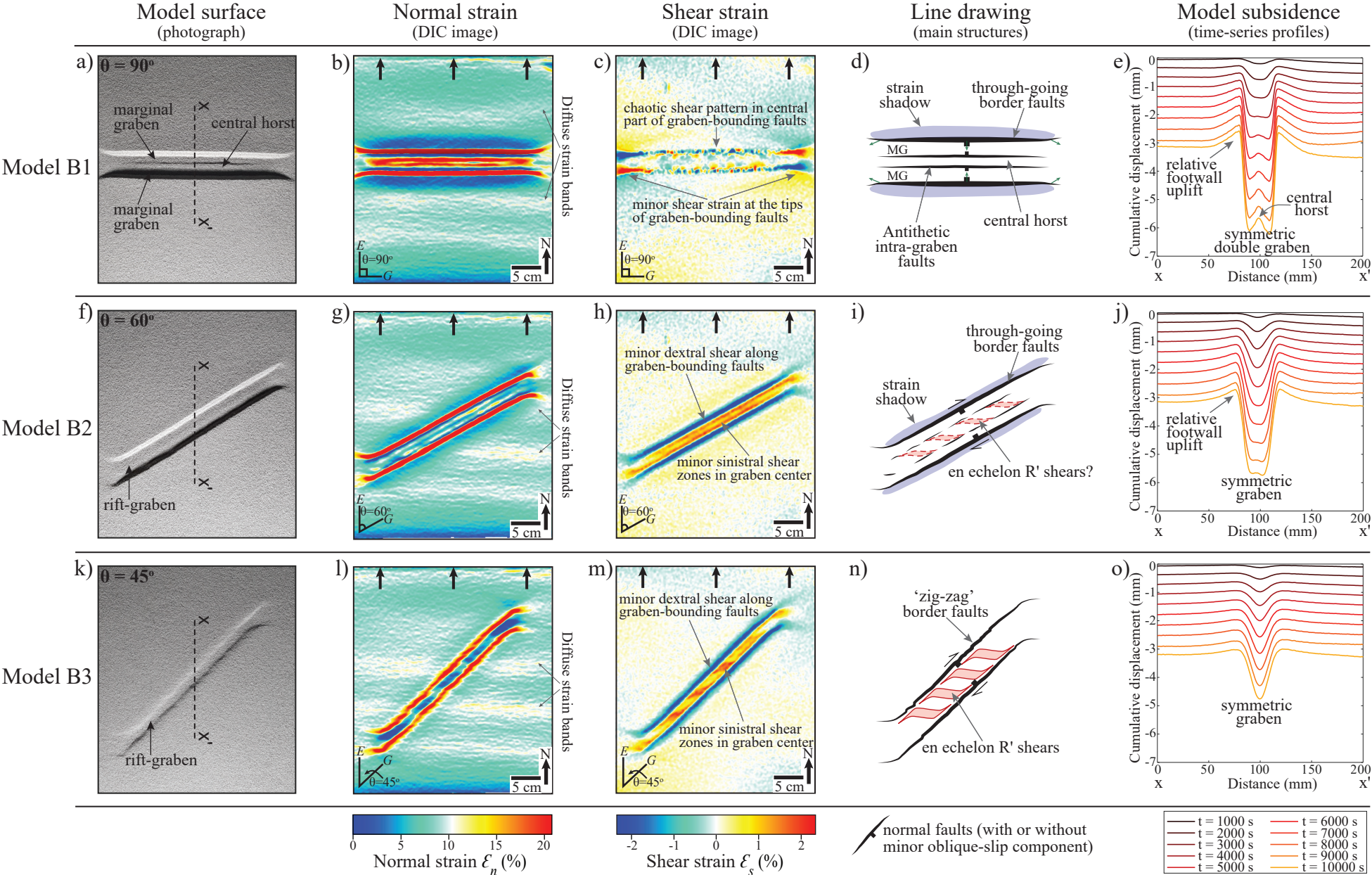


**Figure 5:** Final stage surface deformation of Experimental Series B (large weak zone); Model B1 ( $\theta = 90^\circ$ ), Model B2 ( $\theta = 60^\circ$ ), Model B3 ( $\theta = 45^\circ$ ). Panel consist of photograph of the central portion of model surface, corresponding DIC-derived normal and shear strain components, line drawing of the main normal and shear structures, and time-series model subsidence profiles. Locations of the subsidence profiles are indicated in the photographs (X - X'). The main structures are annotated and lateral exaggeration on the line drawings is 2x. E = extension direction, G = graben axis, t = time in seconds. Note that an apparent 'northern' direction is imposed for the purpose of description.

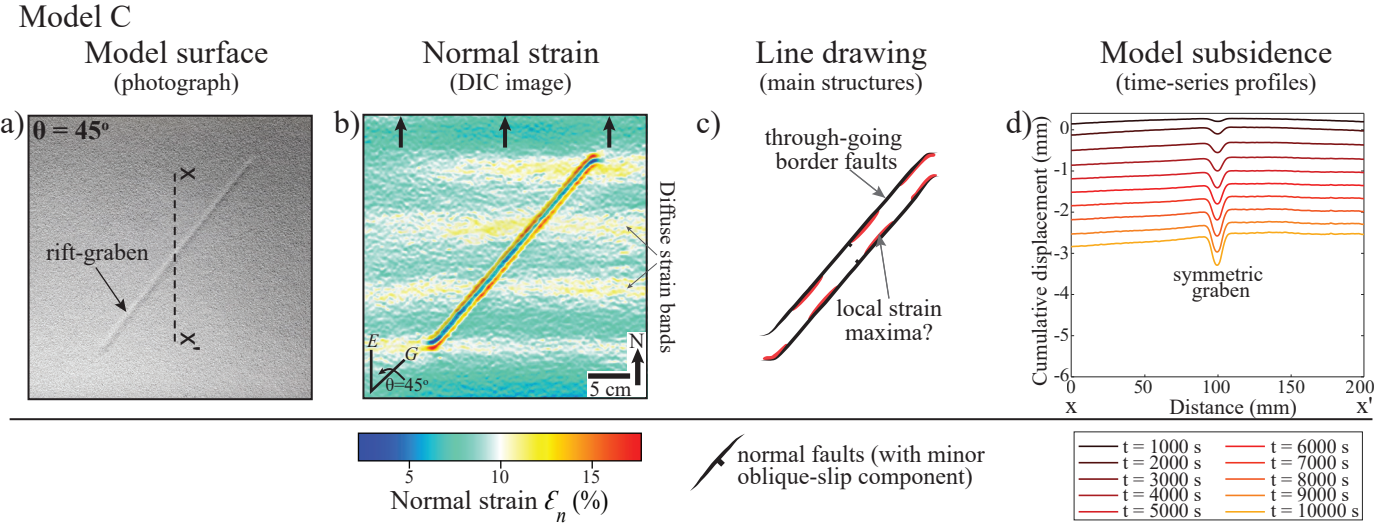


**Figure 6:** Final stage surface deformation of Experimental Series C (thin brittle layer as proxy for shallow weak zone burial); Model C ( $\theta = 45^\circ$ ). Panels consist of (a) photograph of the central portion of model surface, (b) corresponding DIC-derived normal strain component, (c) line drawing of the main structures, and (d) time-series model subsidence profiles. Location of the subsidence profiles in (d) is indicated in (a). The main structures are annotated and lateral exaggeration on the line drawing is 2x. E = extension direction, G = graben axis, t = time in seconds. Note that an apparent ‘northern’ direction is imposed for the purpose of description.



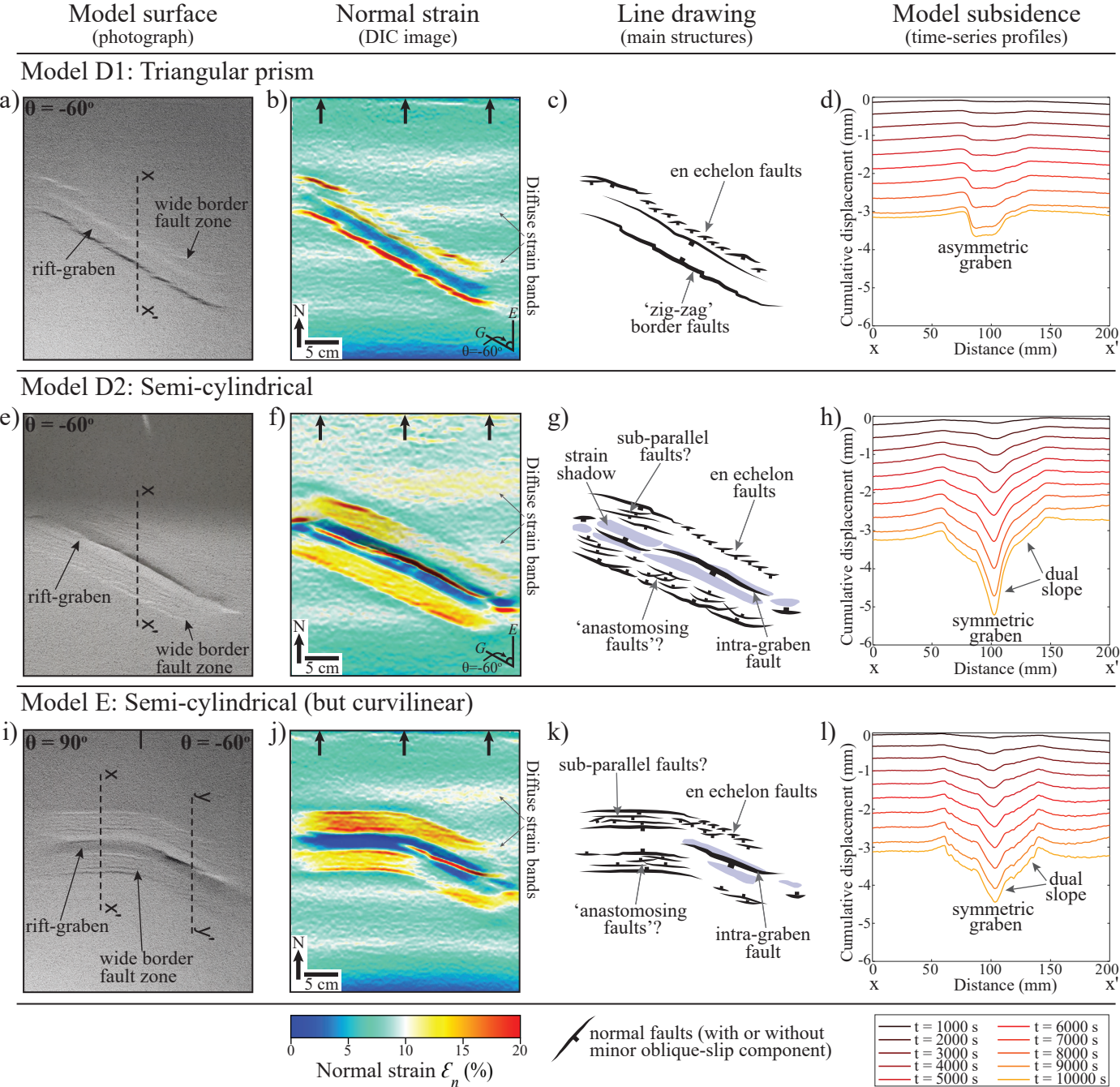


**Figure 7:** Final stage surface deformation of Experimental Series D and E (variable weak zone geometry); Model D1 ( $\theta = -60^\circ$ ), Model D2 ( $\theta = -60^\circ$ ), Model E ( $\theta = 90^\circ$  and  $-60^\circ$ ). Panels consist of photograph of the central portion of model surface, corresponding DIC-derived normal strain components, line drawing of the main structures, and time-series model subsidence profiles. Locations of the subsidence profiles are indicated in the photographs (X - X'). The main structures are annotated. E = extension direction, G = graben axis, t = time in seconds. Note that an apparent 'northern' direction is imposed for the purpose of description.

*Evolution of selected experimental series A and B models*

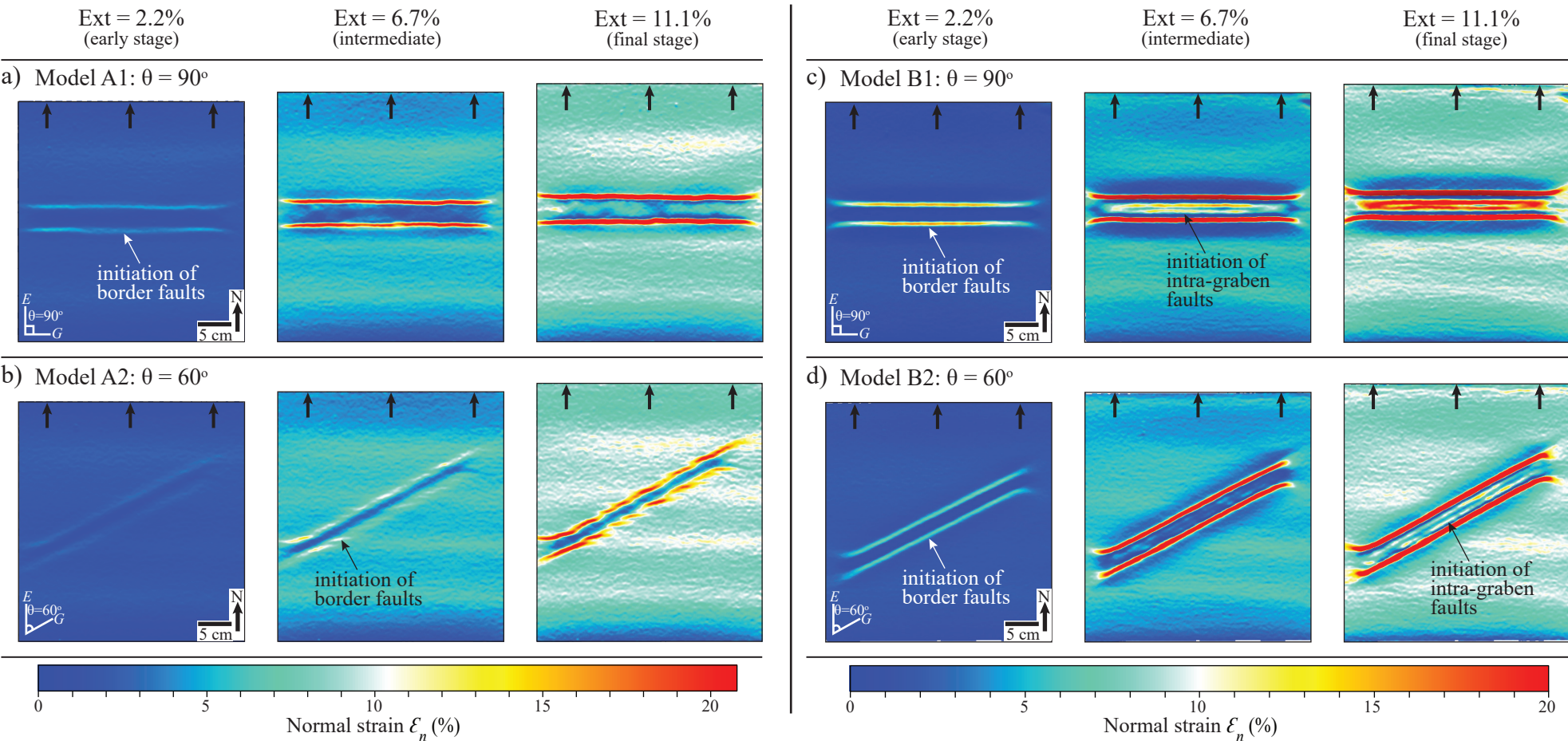


**Figure 8:** Normal strain distribution based on time-series DIC analysis of selected Experimental Series A (small weak zone) and B (large weak zone) models, corresponding to early stage (2.2% extension), intermediate stage (6.7% extension), and final stage (11.1% extension) deformations. (a) Model A1,  $\theta = 90^\circ$ . (b) Model A2,  $\theta = 60^\circ$ . (c) Model B1,  $\theta = 90^\circ$ . (d) Model B1,  $\theta = 60^\circ$ . Note the differences in the timing of initiation and relative amount of strain on the main structures as a function of the orientation and size of the weak zone. E = extension direction, G = graben axis. Note that an apparent ‘northern’ direction is imposed for the purpose of description.

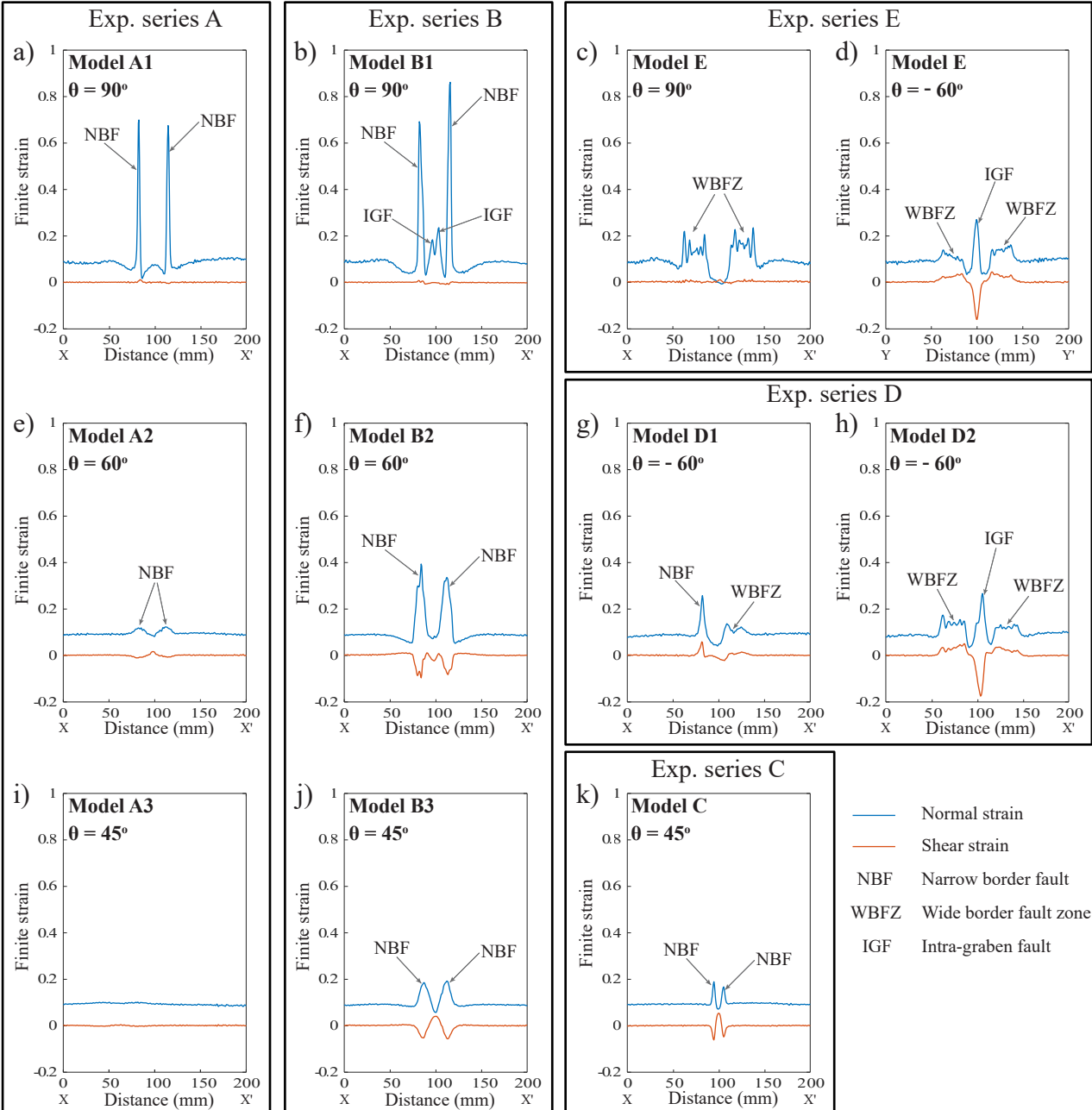


**Figure 9:** Plot of the final stage normal and shear strain components along profile lines that are parallel to the extension direction, and across the main rift structures in all the experimental series. Note that the normal strain is positive indicating extension, whereas the shear strain is either negative (if dextral) or positive (if sinistral). The locations of the profile lines are indicated in Figs. 4,5,6, and 7.

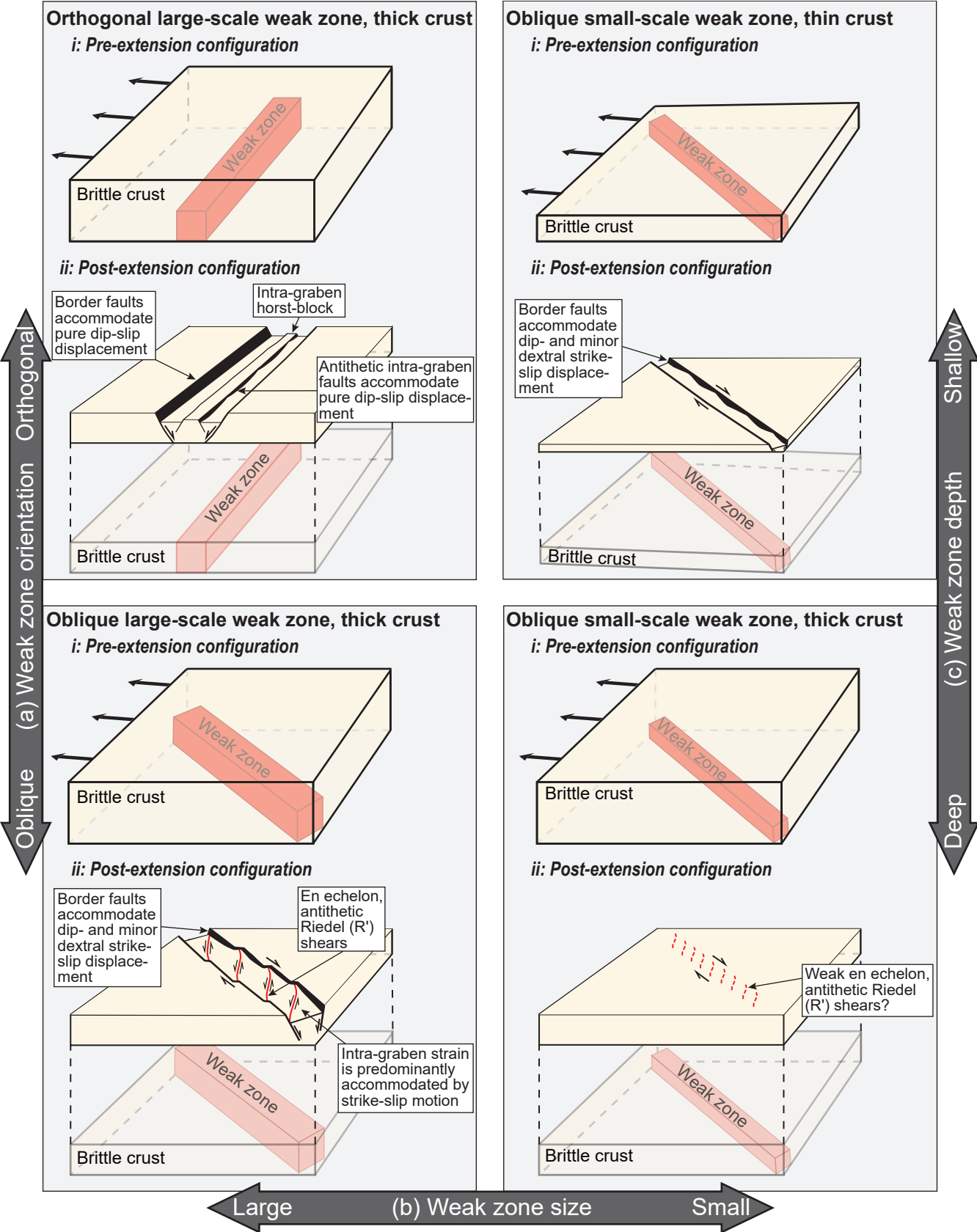


**Figure 10:** Schematic models highlighting the variability in the pattern of strain distribution and localization during rifting. (a) Left column shows variability in strain localization pattern controlled by the orientation of pre-existing weak zones with respect to the extension direction (i.e. orthogonal vs. oblique system), (b) Lower row shows variability in strain localization pattern controlled by the size of pre-existing weak zones, that is, large-scale weak zones exert significant control on the cover faulting pattern, whereas small-scale weak zones exert limited influence, (c) Right column shows variability in strain localization pattern controlled by the thickness of the overburden brittle layer or depth of pre-existing weak zones (not drawn to scale).